Temporal stability and risk analysis of soil slopes subject to rainfall

The influence of heterogeneity

Qian, Cheng; Li, Yajun; Vardon, Philip J.; Shao, Wei; Song, Jiahe; Zhang, Bin; Xu, Nengxiong

DOI
10.1016/j.enggeo.2024.107895

Publication date
2025

Document Version
Final published version

Published in
Engineering Geology

Citation (APA)
Qian, C., Li, Y., Vardon, P. J., Shao, W., Song, J., Zhang, B., & Xu, N. (2025). Temporal stability and risk analysis of soil slopes subject to rainfall: The influence of heterogeneity. *Engineering Geology*, *347*, Article 107895. https://doi.org/10.1016/j.enggeo.2024.107895

Engineering Geology 347 (2025) 107895

Contents lists available at ScienceDirect

Engineering Geology

journal homepage: www.elsevier.com/locate/enggeo

Temporal stability and risk analysis of soil slopes subject to rainfall: The influence of heterogeneity

Cheng Qian [a], Yajun Li [a,b,*], Philip J. Vardon [c], Wei Shao [d,e], Jiahe Song [a], Bin Zhang [a,b], Nengxiong Xu [a,b]

[a] School of Engineering and Technology, China University of Geosciences (Beijing), 29 Xueyuan Road, Beijing, 100083, China
[b] Engineering and Technology Innovation Center for Risk Prevention and Control of Major Project Geohazards, Ministry of Natural Resources, 29 Xueyuan Road, Beijing, 100083, China
[c] Faculty of Civil Engineering and Geosciences, Delft University of Technology, 2628 CN, Delft, The Netherlands
[d] School of Hydrology and Water Resources, Nanjing University of Information Science and Technology, 219 Ningliu Road, Nanjing, 210044, China
[e] Key Laboratory of Hydrometeorological Disaster Mechanism and Warning, Ministry of Water Resources, 219 Ningliu Road, Nanjing, 210044, China

ARTICLE INFO

Keywords:
Rainfall
Unsaturated slopes
Heterogeneity
Temporal stability
Risk analysis

ABSTRACT

Evaluating the temporal stability and risk of unsaturated soil slopes during rainfall is essential for early warning and emergency response to landslides. However, limited research has been conducted on the transition timing of sliding mechanisms, instability/failure time and the integration of sliding consequences into quantitative risk assessment. In order to extend the research in this field, the Random Finite Element Method (RFEM) is used in this paper to investigate the influence of spatial variability of hydraulic properties (related to the fundamental parameter porosity) on the temporal stability and risk of soil slopes subject to rainfall. The findings indicate that the advancing speed of the wetting front is more rapidly in zones with low porosity than in zones with high porosity. As rainfall progresses, the sliding mechanism of the slope shifts from deep sliding to shallow sliding. The homogeneous case tends to underestimate the rise in groundwater levels, leading to an overestimation of slope stability. Hydraulic boundary conditions significantly affect slope stability, making it crucial to consider horizontal (or near the toe of the slope) drainage conditions in practical applications. Additionally, the time of instability/failure predicted in the homogeneous case may be delayed compared to the actual conditions. Both probability of instability/failure and risk increase with continued rainfall. Compared to scenarios where the spatial variability of internal friction angle is not considered, the probability of instability/failure and risk will be higher when the spatial variability of internal friction angle is additionally considered. Risk-based assessment can define the risk levels, reflecting the severity of sliding consequences. Furthermore, the Malin slope failure record from the Chibo region of India is used to validate the effectiveness of the proposed approach. The probabilities of slope failure align well with actual observations, and the risk-based assessment provides additional information into the Malin landslide. This paper proposes a general model for studying the performance of heterogeneous slopes subject to rainfall, providing valuable guidance for landslide early warning systems and the scope and timing of emergency measures taken.

1. Introduction

The field of engineering geology commonly studies natural or artificial soil slopes, and the stability of these slopes is influenced by a combination of internal factors (e.g., soil properties) and external factors (e.g., rainfall, earthquakes). Natural soil slopes often exist in a temporally changing state, with some parts saturated and others partially saturated, and matric suction is a critical factor in maintaining the stability of unsaturated slopes (Cai and Ugai, 2004; Arnold and Hicks, 2011). Climatic conditions can significantly influence slope stability by altering environmental loads, such as rainfall, which subsequently impacts the annual probability of rainfall-induced landslides (Liu and Wang, 2024). When long embankment slopes that are stable in their natural state experience rainfall, the water content and saturation of the shallow zone of the slope increase due to the infiltration of rainwater. This decrease in matric suction reduces the contribution of matric suction to the soil shear strength, ultimately resulting in a significant reduction in slope stability (Zhang et al., 2014; Elia et al., 2017), resulting in rotational or compound slides (Hungr et al., 2014).

---

* Corresponding author at: School of Engineering and Technology, China University of Geosciences (Beijing), 29 Xueyuan Road, Beijing, 100083, China.
E-mail address: y.j.li@cugb.edu.cn (Y. Li).

https://doi.org/10.1016/j.enggeo.2024.107895
Received 10 November 2023; Received in revised form 22 October 2024; Accepted 27 December 2024

Therefore, it is crucial to evaluate the performance of unsaturated slopes under rainfall.

The natural formation process of soil is heterogeneous, making soil a spatially variable material. Therefore, to be most realistic, the parameters used to represent soil properties should also exhibit spatial variability. For instance, internal friction angle, porosity, saturated hydraulic conductivity, and unit weight exhibit spatial variability, and there are often cross-correlations between these parameters. Two methods are typically used to address cross-correlation among multiple parameters: (1) multivariate cross-correlated random property fields (e.g., Arnold (2016), Masoudian et al. (2019)); (2) a single random property field, with other properties related to it (e.g., Le et al. (2015, 2019)). The first method considers the combined effect of the random characteristics of multiple parameters, making it difficult to attribute changes in slope performance to a single parameter, this complexity makes the analysis more challenging. The advantage of the second method is that it can directly present the response of the model to a single parameter.

This spatial variability in soil properties can be effectively described using random fields, often in combination with the Monte Carlo method, forming the Random Finite Element Method (RFEM). RFEM has been shown to enhance our understanding of slope failure mechanisms (Li et al., 2015), which has been used widely to investigate the influence of mechanical parameter variability on slope stability (e.g., Griffiths and Fenton (2004), Hicks and Onisiphorou (2005), Cho (2009), Hicks and Spencer (2010)).

In recent years, many scholars have studied the stability of unsaturated slopes using the RFEM. Le et al. (2015) evaluated how the coefficient of variation (COV) and scale of fluctuation (SOF) of porosity affect the factor of safety (FOS) and failure consequences of unsaturated slopes. Masoudian et al. (2019) considered the spatial variability of porosity to study the stability of brown coal dump sites. Additionally, Liu et al. (2017) found that porosity affects saturated hydraulic conductivity, which in turn influences the stability of unsaturated slopes. These studies emphasise that porosity (or void ratio) is a fundamental parameter for describing soil properties. Variable porosity drives other properties and overall behaviour.

Probability of failure or reliability can be used to evaluate slope performance. Liu et al. (2020) introduced an adaptive Monte Carlo simulation method based on the limit equilibrium method, which significantly improves the computational efficiency in assessing slope failure probability and reliability. However, this method does not account for the influence of rainfall on slope stability. Gu et al. (2023) indicated that the reliability of slopes can be influenced by the uncertainty of soil–water characteristic curve (SWCC) model parameters, and they investigated the response of slope failure probability under different rainfall modes. Similarly, Pan et al. (2024) took into account the spatial variability of saturated hydraulic conductivity (K_s) and shear strength parameters (c' and ϕ') to analyse the failure probability of slopes subjected to rainfall. However, it is important to note that these studies ignore the consequences of failure, and the assessment of slope performance may be incomplete.

The risk assessment of slope failure, which can take into account the impact of the failure consequences, has made significant progress in recent years (Jiang et al., 2022). Typically, risk is expressed as the product of the probability of failure and the consequences of failure. The consequences of failure are influenced by the mode of failure, with deep failures typically resulting in more severe damage, although this depends on the specific situation and chain of events leading to damage. Chowdhury and Xu (1995) and Huang et al. (2010) noted that there may be multiple failure modes for the same slope. For unsaturated slopes, rainwater infiltration reduces matric suction in the unsaturated zone and alters the volumetric weight distribution in the slope, potentially causing shallower or deeper failures. The studies by Le et al. (2015, 2019) confirmed that rainfall infiltration can indeed change the failure mode of slopes. Huang et al. (2013) proposed a new framework for quantitative landslide risk assessment, which is suitable for evaluating the risk of slope failure under various failure modes. Analysing the sliding mechanisms of slopes and assessing slopes temporal stability and risk of failure is essential for early warning systems and the implementation of emergency measures to mitigate the impact of landslides, as highlighted in previous studies (Ju et al., 2020; Yang et al., 2022; Hou et al., 2022; Chansorn et al., 2023).

Arnold (2016) established a transient model subject to rainfall to study the transition of slope failure mechanisms caused by the advancing of the wetting front, and the risk of slope failure had been evaluated. Although these aspects being comprehensively explored, some limitations still exist: (1) it utilised multivariate cross-correlated random property fields, but little is known about the cross-correlation of multivariate random property (limited field evidence) at a particular site; (2) it did not consider the transition timing of sliding mechanisms, which hinders the evaluation of the scope and timing of emergency response to landslides; (3) the impact of rising groundwater levels on slope stability was not investigated due to the hydraulic boundary conditions set; (4) the instability/failure time of heterogeneous slopes was not analysed; (5) the risk of failure was directly estimated from the probability of failure, overlooking the impact of the failure consequences on risk. Addressing these limitations would require further exploration and research.

Additionally, previous research has given less attention to the transition timing of sliding mechanisms and instability/failure time of unsaturated slopes. So far, few articles have attempted to quantify the risk of failure of unsaturated slopes under rainfall over time.

This paper aims to establish a stochastic model for partially saturated soil slopes during rainfall infiltration and quantify the impact of heterogeneous soil parameters on the temporal stability and risk of potential slope instabilities. First, the transient response of an embankment soil slope over a 10 day rainfall period is examined, accounting for the spatial variability of the porosity as a fundamental parameter. The impact of the heterogeneity of hydraulic properties (related to porosity) on the performance of unsaturated slopes is evaluated. Based on Monte Carlo simulation (including 500 random realisations), the distribution of FOS and sliding area are obtained. Each realisation involves different porosity random fields and finite element analyses of the slope. Thereafter, the Malin slope failure record from the Chibo region of India is utilised to validate the effectiveness of the proposed approach. In the following sections, the fundamental methodologies are briefly introduced, including: Richards' equation for water seepage, strength reduction for slope stability, spectral clustering for sliding area quantification, random field for simulating spatial variability, Monte Carlo method for failure probability and risk assessment. Then an illustrative embankment slope example is presented, of which the advancement of the wetting front, changes in groundwater level, FOS and sliding areas/volumes are statistically analysed and discussed. Particularly, the instability/failure time, probability of instability/failure, and a proxy for risk of slope instability are quantified. Subsequently, some conclusions are drawn to highlight the implications of considering the variability of hydraulic soil parameters. Finally, the performance of the Malin slope is analysed using the framework proposed in this paper. The model established in this paper can be used as a general tool for sliding mechanism analysis and quantitative risk assessment of slopes subject to rainfall.

2. Methodology

2.1. Process of the overall analysis

The calculation process of the numerical method is shown in Fig. 1. This study focuses on partially saturated soil slopes subjected to rainfall. The model is implemented in COMSOL Multiphysics, which incorporates both solid mechanics and hydraulic mechanics. A one-way coupled hydraulic–mechanical modelling approach (Vardon et al., 2016)

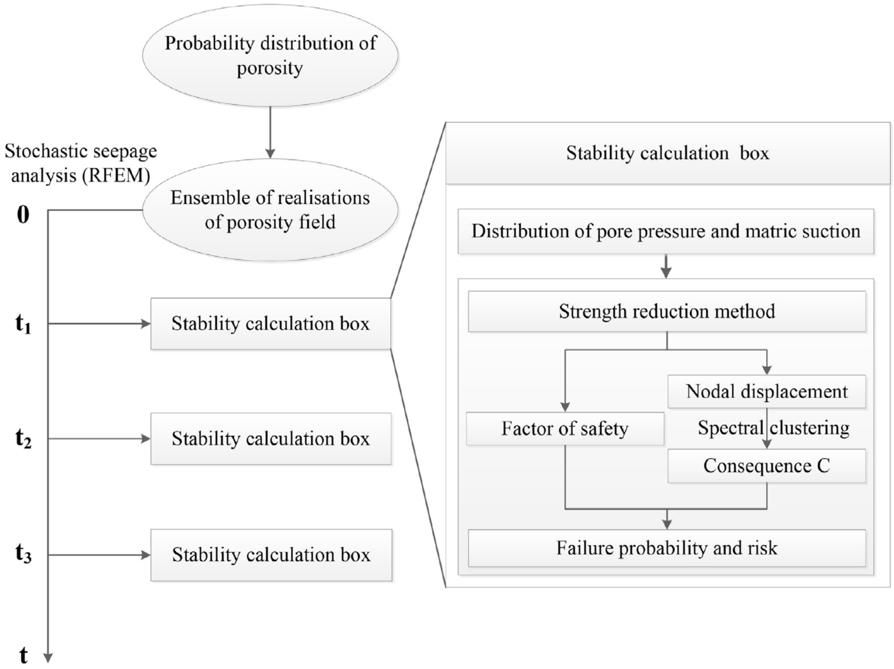

Fig. 1. Numerical approach framework for transient analysis.

is employed, allowing the results of the hydraulic mechanics analysis to inform the subsequent solid mechanics analysis. Firstly, the Local Average Subdivision (LAS) method (Fenton and Vanmarcke, 1990) is used to generate the void ratio (e) random field with spatial variability, which is then transformed into the porosity random field; secondly, the porosity random field is fed into the finite element model, and stochastic seepage analysis is completed to obtain the distributions of pore pressure and effective degree of saturation; thirdly, slope stability analysis is conducted at each rainfall time step to obtain FOS, height of groundwater level, sliding area, etc; finally, the sliding mechanism, time of instability/failure, probability of instability/failure and risk are analysed.

2.2. Transient flow in unsaturated soil slopes

The Richards' equation is used to describe the flow of water in variably saturated porous media:

$$\rho_w\left(\frac{C_m}{\rho_w g}+S_e S\right)\frac{\partial p}{\partial t}+\nabla\cdot\rho_w\left(-\frac{K_s}{\mu_w}K_r(\nabla p+\rho_w g\nabla D_e)\right)=Q_m \tag{1}$$

where C_m is the specific moisture capacity, as shown in Eq. (6); S_e is the effective degree of saturation; S is the water storage coefficient; K_s is the saturated hydraulic conductivity; K_r is the relative hydraulic conductivity; ρ_w is the fluid density; g is the acceleration of gravity; μ_w is the viscosity of water; p is the water pore pressure; t is the time; D_e is the elevation; Q_m is the fluid source (positive) or sink (negative), as shown in Eq. (2), u is the fluid velocity; and ∇ represents the gradient operator. The hydraulic conductivity of unsaturated soil can be defined as Eq. (3)

$$\nabla\cdot(\rho_w u)=Q_m \tag{2}$$

$$K=K_r K_s \tag{3}$$

The SWCC is used to describe the relationship between matric suction and volumetric water content. There are many fitting equations that describe the SWCC of unsaturated soils, with the van Genuchten (VG) model and the Fredlund and Xing (FX) model being the most widely used.

The SWCC and relative hydraulic conductivity are described by the VG model (Van Genuchten, 1980):

$$S_e=\begin{cases}\frac{\theta_w-\theta_r}{\theta_s-\theta_r}=\frac{1}{\left(1+|\alpha_{VG}p|^{n_{VG}}\right)^{m_{VG}}} & p<0\\ 1 & p\geq 0\end{cases} \tag{4}$$

$$K_r=\begin{cases}\sqrt{S_e}\left[1-\left(1-S_e^{\frac{1}{m_{VG}}}\right)^{m_{VG}}\right]^2 & p<0\\ 1 & p\geq 0\end{cases} \tag{5}$$

$$C_m=\begin{cases}\frac{\alpha_{VG}m_{VG}}{1-m_{VG}}(\theta_s-\theta_r)S_e^{\frac{1}{m_{VG}}}(1-S_e^{\frac{1}{m_{VG}}})^{m_{VG}} & p<0\\ 0 & p\geq 0\end{cases} \tag{6}$$

where θ_w, θ_s and θ_r are the volumetric water content, saturated volumetric water content, and residual volumetric water content, respectively; α_{VG}, m_{VG} and n_{VG} are fitting parameters for the VG model, and $m_{VG}=1-1/n_{VG}$.

The SWCC and relative hydraulic conductivity are described by the FX model and Leong and Rahardjo model (Pan et al., 2024):

$$\theta_w=\frac{\theta_s}{\left\{\ln\left[e_{eluer}+\left(\alpha_{FX}p\right)^{n_{FX}}\right]\right\}^{m_{FX}}} \tag{7}$$

$$K_r=\left(\frac{\theta_w}{\theta_s}\right)^{p_k} \tag{8}$$

where α_{FX}, m_{FX} and n_{FX} are fitting parameters for the FX model; e_{eluer} is the Euler's number; p_k is the constant related to the soil type.

The parameter α_{VG} and α_{FX} can be related to porosity (ϕ), and utilises an additional parameter η (Rodríguez et al., 2007; Zandarín et al., 2009):

$$\alpha_{VG/FX}=\frac{\alpha_{s0}}{\exp[\eta(\phi_0-\phi)]} \tag{9}$$

where ϕ_0 is the base value of porosity; ϕ is the porosity; and the parameter η controls the rate at which $\alpha_{VG/FX}$ deviates from its base value α_{s0} when ϕ deviates from its base value ϕ_0. Similarly, saturated hydraulic conductivity can be related to porosity (ϕ) by using the

Kozeny equation (Le et al., 2015):

$$K_s = K_{s0}\frac{\phi^3}{(1-\phi)^2}\frac{(1-\phi_0)^2}{\phi_0^3} \tag{10}$$

where K_{s0} is the base value of the saturated hydraulic conductivity.

2.3. Slope stability analysis

The extended Bishop's effective stress criterion (Bishop and Blight, 1963) and the Mohr–Coulomb (MC) model are used here to describe the mechanical constitutive behaviour of unsaturated soils. The failure criterion for unsaturated soil is:

$$\tau_f = c' + (\sigma_t - u_a)\tan\phi' + \chi(u_a - u_w)\tan\phi' \tag{11}$$

where τ_f is the soil shear strength; c' is the effective cohesion; ϕ' is the effective internal friction angle; σ_t is the total stress; u_a is the pore air pressure; u_w is the pore water pressure; χ is the effective stress parameter equal to the effective degree of saturation; (σ_t-u_a) is the net stress; (u_a-u_w) is the matric suction; and $\chi(u_a - u_w)$ is the suction stress. Eq. (11) reflects the contributions of net stress, matric suction, effective cohesion and effective internal friction angle to the strength of unsaturated soils, the suction stress decreases with the decrease of matric suction.

The strength reduction method (SRM) is used to calculate the FOS and to monitor the maximum displacement response of the slopes. The effective cohesion and the tangent of the effective internal friction angle are simultaneously divided by the reduction factor, as shown in Eq. (12), where c'_{fail} and ϕ'_{fail} represent the effective cohesion and the effective internal friction angle when the strength parameters are reduced to slope failure.

$$FOS = \frac{c'}{c'_{fail}} = \frac{\tan\phi'}{\tan\phi'_{fail}} \tag{12}$$

The slope is considered stable when the FOS is greater than the critical factor of safety (CFOS), and unstable when the FOS is less than the CFOS (especially when CFOS=1, slopes with FOS less than CFOS are considered to have failed):

$$\begin{cases} \text{Stable} & FOS > CFOS \\ \text{Unstable} & FOS \le CFOS \end{cases} \tag{13}$$

2.4. Generation of spatially variable properties

The statistical characteristics of soil parameters can describe the probability distribution of variables, such as mean (μ), standard deviation (σ) or COV (COV=σ/μ). SOF (θ) is used to characterise the distance between spatial points within which soil parameters show a relatively strong correlation. Here the LAS (Fenton and Vanmarcke, 1990) is used to generate random fields. This method generates a standard normal random field which can be transformed to an appropriate target distribution (e.g., the log-normal distribution). In addition, the field values can be post-processed to obtain anisotropic random fields to represent different SOFs in different directions (Hicks and Samy, 2004). The correlation structure of the soil property is characterised by a simple exponential correlation function:

$$\rho(\tau_1,\tau_2) = \exp\left(-\sqrt{\left(\frac{2\tau_1}{\theta_1}\right)^2 + \left(\frac{2\tau_2}{\theta_2}\right)^2}\right) \tag{14}$$

where (τ_1, τ_2) is the lag distance between two points in a random field, and the subscripts 1 and 2 represent the vertical and horizontal coordinate directions, respectively.

2.5. Failure probability and risk

Consequence of failure is an important factor in the risk assessment of slope failure (Zhang and Huang, 2016). The risk R is defined as (Huang et al., 2013):

$$R = \sum_{i=1}^{n_f} p_{fi} \times C_i = p_{fi}\sum_{i=1}^{n_f} C_i = \frac{1}{n_{real}}\sum_{i=1}^{n_f} C_i \tag{15}$$

where p_{fi} and C_i are the probability and consequence of failure mode i, respectively, and n_f is the number of failure cases in a Monte Carlo simulation. The failure modes of each realisation are independent of each other, so the probability of a single failure mode is constant, i.e., $p_{fi} = 1/n_{real}$, where n_{real} is the total number of realisations.

The options used to represent the impact of slope failure include the volume of the failure mass, the height of the failing mass relative to the ground, the distance from the slope toe to the element at risk, or aspects relating to the dynamic behaviour of sliding masses, such as velocity and energy (Cui et al., 2022). However, the analysis of the consequences of slope failure is highly dependent on the analysis method. For an ideal two-dimensional slope model, the choice of the sliding area as a proxy for the failure consequences is an acceptable result.

2.6. Slope sliding area calculation

Huang et al. (2013) and Le et al. (2015) identified two typical slope failure modes: shallow failure and deep failure. They used nodal displacements of the slope to identify the landslides and calculate the sliding area. Additionally, Hicks et al. (2014) used a simpler method to determine the failure consequences of 3D slopes by recording the maximum x-direction nodal displacement in the mesh, and for a given percentage of the maximum displacement, the volume of the mesh greater than or equal to this displacement is calculated. The nodal displacements of the slope can therefore be used to quickly and easily identify the landslide.

The use of any predefined displacement threshold to identify landslides is not generalisable. From a classification perspective, landslides can be identified without using such a threshold. The spectral clustering method works well for the application considered in this paper. It conceptualises all data as points in a high-dimensional space, connected by edges that representing their similarities. A similarity matrix is constructed to quantify the connections between these points, and then the eigenvalues and eigenvectors of the graph Laplacian are used to identify a partitioning of the data. This partitioning is characterised by high intra-cluster similarity and low inter-cluster similarity, thereby achieving the purpose of clustering.

The nodal displacements are classified by spectral clustering to obtain the sliding area. Spectral clustering can be summarised into three steps (Bojchevski et al., 2017): (a) First, the k-nearest neighbour (KNN) method is used to generate a similarity graph $\boldsymbol{A}$; (b) The normalised-cut method (Ncut) is used to cut the graph $\boldsymbol{A}$ into k_p unconnected subgraphs; (c) Finally, the K-means clustering method is used to obtain the final classification result.

The SRM is used to calculate the FOS of the slope, and the displacements of the finite element nodes are collected when the iteration to find the elastic–plastic strain variable does not converge. Figs. 2(a) and 2(c) are the displacement distributions of the slope under the limit state (failure), corresponding to the shallow sliding and deep sliding of the slope. Figs. 2(b) and 2(d) show the classification results, with the sliding mass marked in red. The size of the sliding area is used as a criterion for classifying the slope sliding modes, this value is shown in Section 3.4.

3. Illustrative example 1: an embankment slope

Griffiths and Lu (2005) analysed the stability of homogeneous slopes composed of silt and clay. Their findings indicated that the stability of silt slopes was more susceptible to rainfall infiltration. It is therefore necessary to carry out a transient rainfall infiltration analysis for heterogeneous silt slopes. In this section, a representative clayey silt embankment slope subject to rainfall is considered.

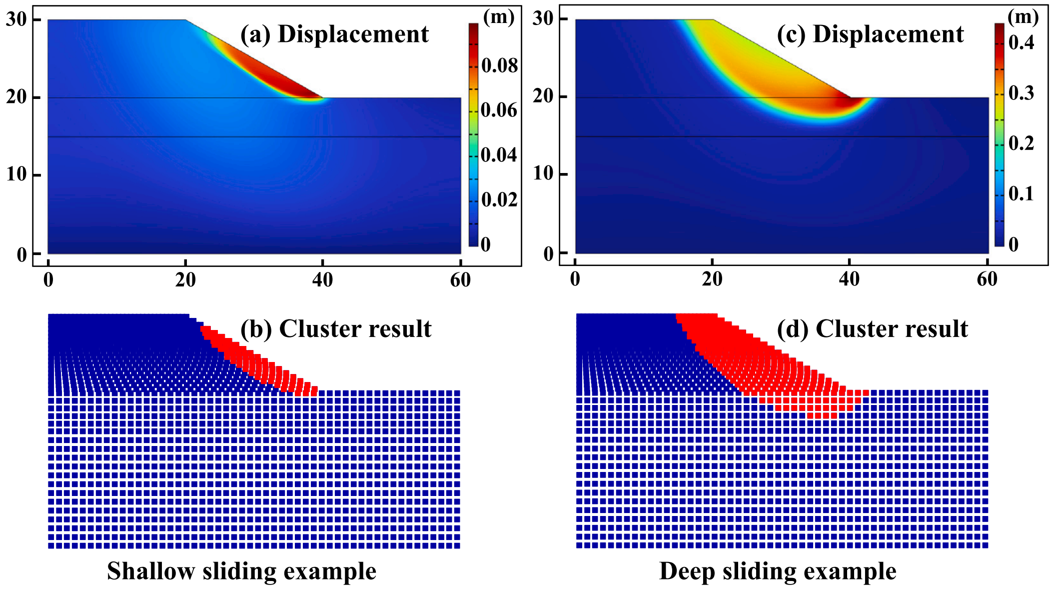

Fig. 2. Spectral clustering results: (a, c) slope displacement at failure for two examples; (b, d) classification results of shallow failure and deep failure (sliding mass is red). (For interpretation of the references to colour in this figure legend, the reader is referred to the web version of this article.)

3.1. Slope description

The slope has a height of 10 m, resting on a 20 m thick base, and the slope ratio (vertical direction to horizontal direction) is 1:2. The slope geometry and boundary conditions are shown in Fig. 3. The finite element model adopts second-order quadrilateral elements, with the maximum side length of the elements being 1.2 m. It consists of 1564 elements, which has been verified to meet the accuracy requirements for the calculations.

The numerical modelling is representative of possible in situ conditions. The two sides (ABC and FGH) of the model are assigned roller boundary conditions (zero x-displacement), while a fixed boundary condition at the bottom (AH) with zero x-displacement and y-displacement. The initial groundwater level is set at 15 m (5 m below the toe of the slope), while the free water surface outside the slope is located at point G. The pore air pressure is assumed to be constant and equal to the atmospheric pressure, then the suction equal to the negative value of pore water pressure. Thus, the maximum initial matric suction occurs at the top of the slope under static water conditions (150 kPa). A no-flow boundary condition is applied along AH, BC and FG, while a Dirichlet seepage (e.g., Masoudian et al. (2019)) was prescribed along GH, where a constant pressure head is maintained. Groundwater exceeding the set head can flow out of the slope through GH.

Arnold (2016) found that the failure probability of ultimate limit state may increase significantly for slopes subjected to prolonged periods of low-intensity rainfall. Additionally, Liu et al. (2023) developed an explicit relationship between rainfall intensity and duration (i.e., the critical rainfall pattern curve (CRPC)) for a specific slope and found that the CRPCs obtained from the uniform and stochastic rainfall models were generally consistent. In this paper, a slope subject to 10 days of “relatively small” uniform rainfall events is examined, with rainfall boundary conditions applied along CDEF with an infiltration rate of q (43.2 mm/d). Furthermore, the pore pressure along the CDEF is not allowed to exceed zero, which means that rainfall beyond the infiltration capacity will not enter the model domain and will not accumulate at the slope toe. To investigate the detailed changes in slope stability during rainfall, a total of 40 slope stability calculations were performed, corresponding to 0.25 day per time step. Even if the FOS of the slope drops to 1.0 at a particular rainfall instant, stability calculations are still performed for subsequent time steps to capture the full process of slope stability changes over time.

The VG model was used to describe the SWCC and relative hydraulic conductivity. The statistical characteristics of typical clayey silt soil properties are shown in Table 1. To avoid deviating from the typical values, the m_{VG}, η and α_{s0} are approximately the middle of their respective typical ranges of variation (Bear, 1972; Van Genuchten, 1980; Zandarín et al., 2009). It should be noted that the framework used in this paper can also be applied to analyse other types of soil slopes.

Some studies have reported values of saturated hydraulic conductivity of silt soils ranging from 1×10^{-5} m/s to 4.4×10^{-5} m/s (Wang et al., 2018; Ng et al., 2022). Le et al. (2019) found that for typical clayey silt soils, a larger K_{s0} (e.g., 10^{-4} m/s) facilitates water flow, resulting in a smaller pore pressure gradient and a reduced decrease in matric suction, leading to a smaller decrease in shear strength. Conversely, a lower K_{s0} (e.g., 10^{-6} m/s) limits infiltration and restricts water movement along the slope to very shallow layers. Therefore, the base value of the saturated hydraulic conductivity is set to $K_{s0} = 10^{-5}$ m/s (flow ratio $q/K_{s0} = 0.05$), which produces a large pore pressure gradient and a significant suction drop, allowing the sliding surface to remain within the wetted region of the shallow surface.

Eq. (11) demonstrates that both matric suction and shear strength parameters contribute to slope stability. The heterogeneity of porosity affects the hydraulic properties of the slope, which in turn influences the distribution of matric suction and ultimately impacts the strength of the soil. The determination of shear strength parameters is also influenced by porosity. Mouyeaux et al. (2018) indicated that slope stability is particularly sensitive to strength parameters, especially the internal friction angle. The subsequent sections analyse the influence of porosity on hydraulic properties, which in turn affects the distribution of matric suction and ultimately affects slope performance. To isolate this influence from other factors, it is assumed that the stiffness and strength of the soil remain constant. In addition, the scenario of considering the spatial variability of both hydraulic properties and internal friction angle are presented in Appendix A.

The values of c' and ϕ' used in this study are typical values for clayey silts, as reported by Bishop et al. (1960). Young’s modulus (E) and Poisson’s ratio (ν) are also within the typical range for clayey silt soils (Zhu, 2014). It should be noted that the random variability of the void ratio (e) is introduced before the application of gravity to account for the effect of the variation in soil unit weight (caused by

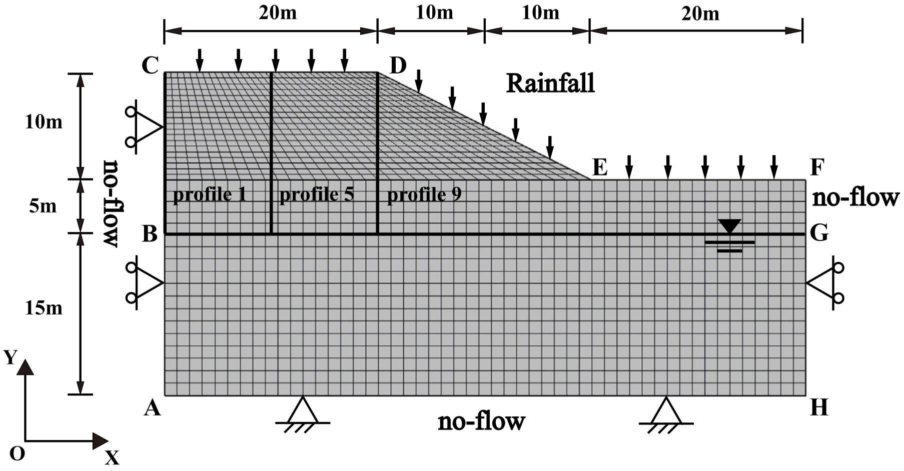

Fig. 3. Model size and elements (profiles 1, 5 and 9: for analyses in Section 3.2).

Table 1
Soil parameter values.

Parameter	m_{VG}	η	ϕ_0	K_{s0}	α_{s0}	E	ν	c'	ϕ'
Value	0.2	5	0.333	10^{-5}	0.05	100 000	0.3	4	16
Units	–	–	–	m/s	1/kPa	kPa	–	kPa	°

Table 2
Statistical characteristics of the random parameter (void ratio).

Distribution type	Mean	COV	Vertical SOF (m)	Horizontal SOF (m)	Anisotropy	Number of realisations
Log-normal	0.5	0.3	8.0	32.0	4	500

the variability of e) on the initial stress distribution.

There are very few published real measurement values of the SOF for void ratio. Le et al. (2013, 2019) investigated the SOF for the void ratio of clayey silts and used SOF(e) = 8 m in the study, but without considering soil anisotropy. Furthermore, Phoon and Kulhawy (1999) found that the horizontal SOF of soil properties is more than one order of magnitude larger than the vertical SOF. Eq. (10) shows that porosity is correlated with saturated hydraulic conductivity, many studies (e.g., Liu et al. (2018)) have shown that the horizontal SOF is considerably greater than the vertical SOF for saturated hydraulic conductivity in layered clay soils, implying that the horizontal SOF for porosity is similarly greater than the vertical correlation length. Given this limited information, the statistical parameters of the void ratio used in this study are presented in Table 2. Assuming that the void ratio follows a log-normal distribution to ensure the values of the void ratio are positive, and the anisotropic random field of the void ratio is converted into the anisotropic random field of the porosity to ensure that the obtained porosity value remains between 0 and 1.

Fig. 4(a) shows the typical porosity random field for realisation 1, Fig. 4(b) shows the random field of parameter α_{VG} (VG model) according to Eq. (9), and Fig. 4(c) shows the random field of saturated hydraulic conductivity according to Eq. (10). Figs. 4(d–f) show the typical random field of porosity, α_{VG} and saturated hydraulic conductivity for realisation 2. It is evident from Figs. 4(a–c) that α_{VG} and saturated hydraulic conductivity are larger in zones where porosity is higher. Additionally, Fig. 4(d) illustrates that the porosity in zone 1 is lower than in zone 2, which will affect the advancing speed of the wetting front, as discussed in Section 3.2.

3.2. Wetting front

According to the improved Green–Ampt model (Jiang et al., 2023), the soil profile can be divided into two regions during rainfall infiltration: a wetting region (including the transition region) and a non-wetting region. The interface between the two regions is termed the wetting front. This means that the soil below the wetting front is at the initial degree of saturation. Similarly, in this paper, the interface is treated as the wetting front, which between the region with a change in effective degree of saturation and the region without a change in effective degree of saturation. Rainfall infiltration increases the effective degree of saturation in the shallow surface soil of the slope. Under the influence of gravity, water is transported towards the interior of the slope, resulting in the formation of a wetting front that progresses inwards as rainfall continues.

Fig. 5 illustrates the distribution of the effective degree of saturation, the wetting front, and the sliding surface for two typical realisations and the homogeneous case at different stages of rainfall (T= 0th, 1st, 5th and 10th day). Prior to the onset of rainfall, the initial distribution of the effective degree of saturation generated by the initial suction profiles (according to Eq. (4)) is shown in Figs. 5(a), 5(e) and 5(i). The spatial variability of the porosity results in a non-uniform initial distribution of the effective degree of saturation and leads to heterogeneous rainfall infiltration, which is more evident in Figs. 5(e–h). As shown in Fig. 4(d), the porosity in zone 1 is generally smaller than that in zone 2, and Fig. 5(h) indicates that the wetting front advances faster in zone 1 compared to zone 2, suggesting that the wetting front advances faster in zones with lower porosity.

On the 10th day of rainfall, 9 profiles were selected to investigate the relationship between the advancing depth of the wetting front and the average porosity of the profile above the wetting front. The coordinates of the profiles are listed in Table 3. Fig. 6 shows a negative correlation between the advancing depth of the wetting front and the average porosity of the profile above the wetting front. This suggests that profiles with lower porosity result in a faster advancement of the wetting front.

Figs. 7(a–b) show the relationship between the effective degree of saturation and the unsaturated hydraulic conductivity with matric suction. The maximum matric suction of the slope in this paper is 150

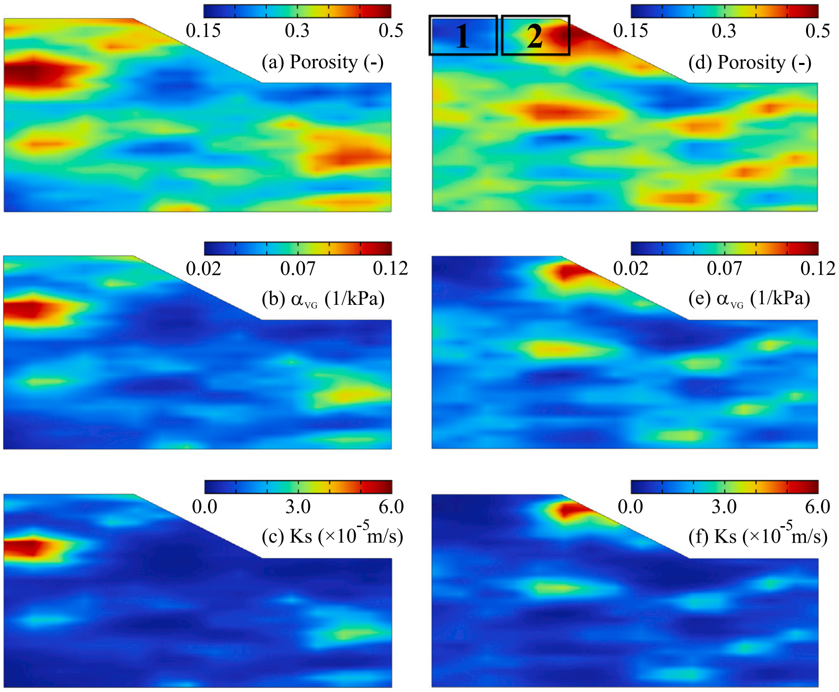

Fig. 4. Two typical random realisations: (a, d) field of porosity; (b, e) field of α_{VG} (VG model); (c, f) field of saturated hydraulic conductivity (zones 1 and 2 are employed to facilitate a comparative analysis of the distribution of porosity).

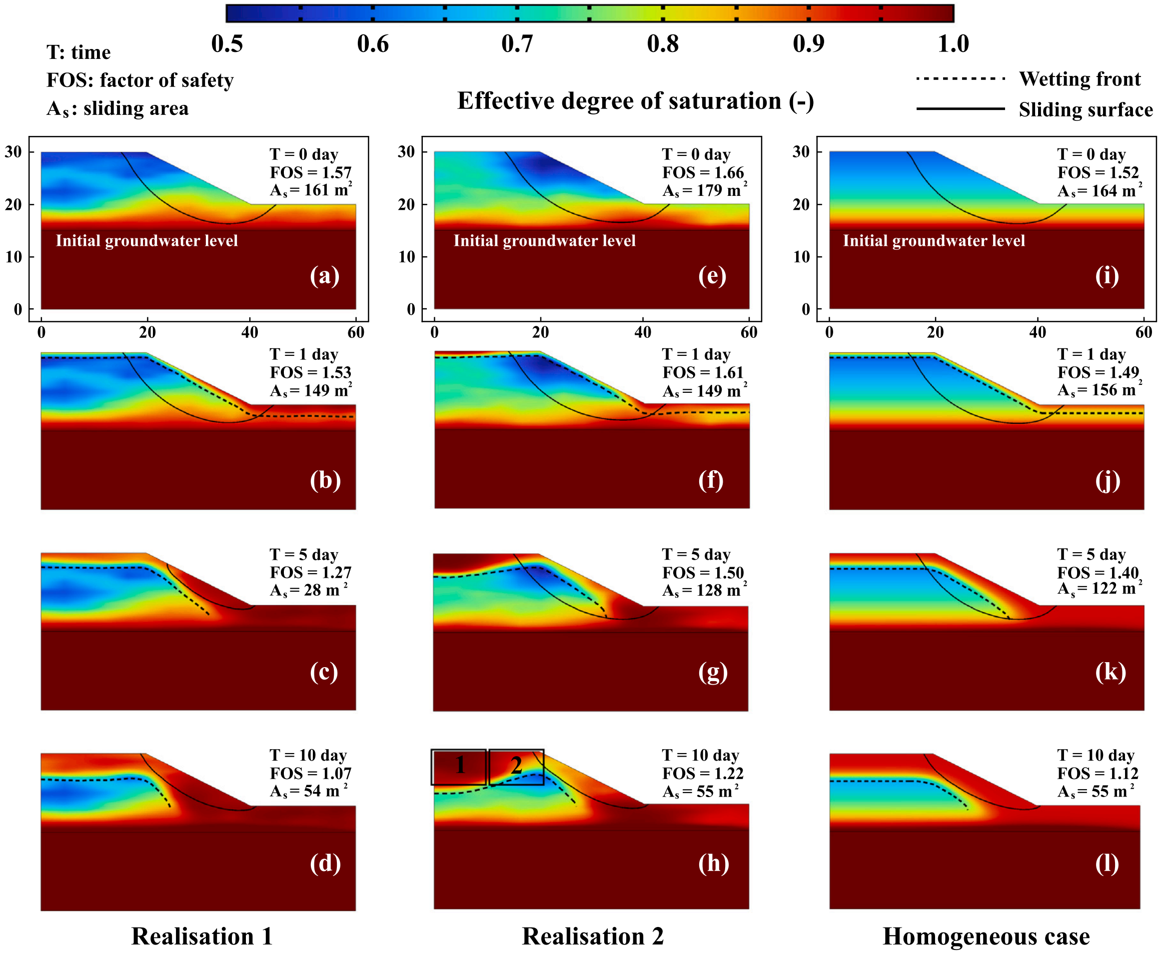

Fig. 5. Distribution of effective degree of saturation, wetting front (dashed line) and sliding surface (solid line): (a–d) realisation 1; (e–h) realisation 2; (i–l) homogeneous case (zones 1 and 2 are used to assess the advancing speed of the wetting front).

Table 3
The coordinates of the start and end points of the profiles (examples of profiles 1, 5 and 9 are shown in Fig. 3).

Profile	Start point	End point
1	(0,15)	(0,30)
2	(2.5,15)	(2.5,30)
3	(5,15)	(5,30)
4	(7.5,15)	(7.5,30)
5	(10,15)	(10,30)
6	(12.5,15)	(12.5,30)
7	(15,15)	(15,30)
8	(17.5,15)	(17.5,30)
9	(20,15)	(20,30)

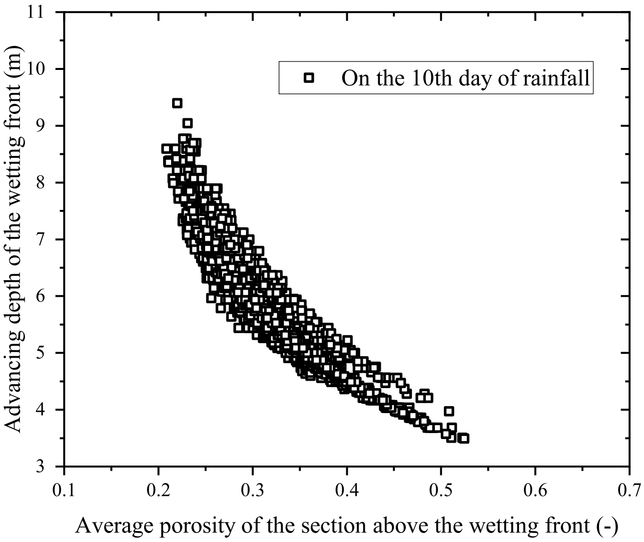

Fig. 6. Advancing depth of the wetting front versus average porosity.

kPa, and the matric suction at an effective degree of saturation of 0.82 is 30 kPa. The approximate range of matric suction variation in this paper is indicated by a dashed box in Figs. 7(a–b). The effective degree of saturation varies significantly for different porosity values, as indicated by the dashed box in Fig. 7(a). In addition, there is little difference in unsaturated hydraulic conductivity for porosity values greater than 0.2, as shown in the dashed box of Fig. 7(b).

The dry density of the specimen is controlled by the void ratio (porosity). Through physical experiments, Wang et al. (2023) found that the void ratio (porosity) mostly controls the permeability. For the specimen after the first rainfall, the unsaturated permeability is insensitive to changes in the dry density of specimens when the volumetric water content is less than 0.12. In other words, the unsaturated permeability is insensitive to changes in porosity at this time. When the volumetric water content exceeds 0.12, specimens with different dry densities have similar unsaturated permeability at the same volumetric water content. This is similar to the conclusion of this study.

Figs. 7(c–d) show the initial hydraulic conductivity distribution for two typical realisations. Although zone 2 has a higher porosity than zone 1 (Fig. 4(d)), the unsaturated hydraulic conductivities of zone 1 and zone 2 in Fig. 7(d) are not significantly different. In the saturated zone (the region below the groundwater level), the saturated hydraulic conductivity increases with increasing porosity.

Zones with low porosity contain a smaller proportion of pores within the total volume of the soil. Over the same rainfall duration, low porosity zones have a greater proportion of soil with changes in initial effective saturation, indicating that the wetting front advances deeper into the soil. This paper examines the advancing speed of the wetting front, which is influenced by the combined effect of distribution of porosity and unsaturated hydraulic conductivity, with porosity being the primary factor.

If only the spatial variability of the saturated hydraulic conductivity is considered and the porosity is assumed to be constant, the opposite conclusion may be reached. This highlights the importance of selecting fundamental parameter carefully. In areas where the wetting front advances more rapidly, the matric suction disappears more rapidly, it is clear that more attention should be paid to areas with lower porosity.

Prior to the onset of rainfall, the matric suction of the unsaturated soil contributes significantly to slope stability, and the slope has the highest FOS and maximum sliding area at this time. The potential sliding mechanism of the slope exhibits a deep sliding. At the beginning of the rainfall (as shown in Figs. 5(b) and 5(f)), only the superficial soil layer is wetted. As rainfall continues until the 5th day (Fig. 5(c)), the shallow soil tends to become saturated, reducing the contribution of matric suction to slope stability and resulting in a decrease in shear strength. Failure occurs primarily in the shallow areas with a smaller sliding area.

In Fig. 5(g), the presence of matric suction at the slope shoulder proves to be beneficial for slope stability, allowing the slope to maintain a deep sliding mechanism. The FOS decreased from 1.53 to 1.27 between Figs. 5(b–c), and the FOS decreased from 1.61 to 1.50 between Figs. 5(f–g). A sudden decrease in FOS is observed when the sliding mechanism is changed.

3.3. *Factor of safety*

Fig. 8 shows a heat map of the FOS consisting of the probability density function (PDF) of the FOS at each rainfall time step. Specifically, the PDFs of the FOS on the 1st, 5th and 10th day are shown as 'deterministic' in Fig. A.22. The colour bar in Fig. 8 is a local colour bar, with red indicating a higher frequency of FOS. The upper limit of 100 is set to better represent the frequency distribution of FOS throughout the rainfall period.

The 'deterministic' results in Fig. A.22 indicate that the normal distribution provides a reasonable fit to the Monte Carlo simulation outcomes on the 1st and 10th days, while the fit on the 5th day is poor due to changes in the sliding mechanism of some slopes within the Monte Carlo simulation. As shown in Figs. 5(b–c), the FOS decreases significantly during this period, leading to greater variability in the FOS.

In general, Fig. 8 illustrates that the FOS decreases as rainfall progresses. The FOS obtained from the homogeneous case is often larger than the mode of the FOS obtained from the Monte Carlo simulation, suggesting that the homogeneous case may generally overestimate the slope stability. The distribution of FOS is relatively narrow (with a small standard deviation) for the 0–3 days and 8–10 days periods. However, the distribution of FOS is wider between 3–8 days. This is because during 3–8 days of rainfall, some realisations experience a change in their sliding mechanism from deep to shallow sliding. This change causes a sharp decrease in FOS, resulting in an increase in the standard deviation. Therefore, the variability of the FOS of the slope is greatest during the middle stage of the rainfall.

3.4. *Sliding consequence*

Fig. 9 shows the heat map of the sliding area, which consists of multiple PDFs of the sliding area. In particular, the PDFs of the sliding area on the 1st, 5th and 10th day are shown as 'deterministic' in Fig. A.23. The colour bar in Fig. 9 is a local colour bar.

According to Section 3.2, the analysis indicates that as the advancing of wetting front, local areas will develop between the wetting front and the slope surface. In the local areas, the soil was wetted and the saturation increased, resulting in a decrease in matric suction and lower shear strength; at the same time, the total weight of the soil increases, which increases the overturning moment.

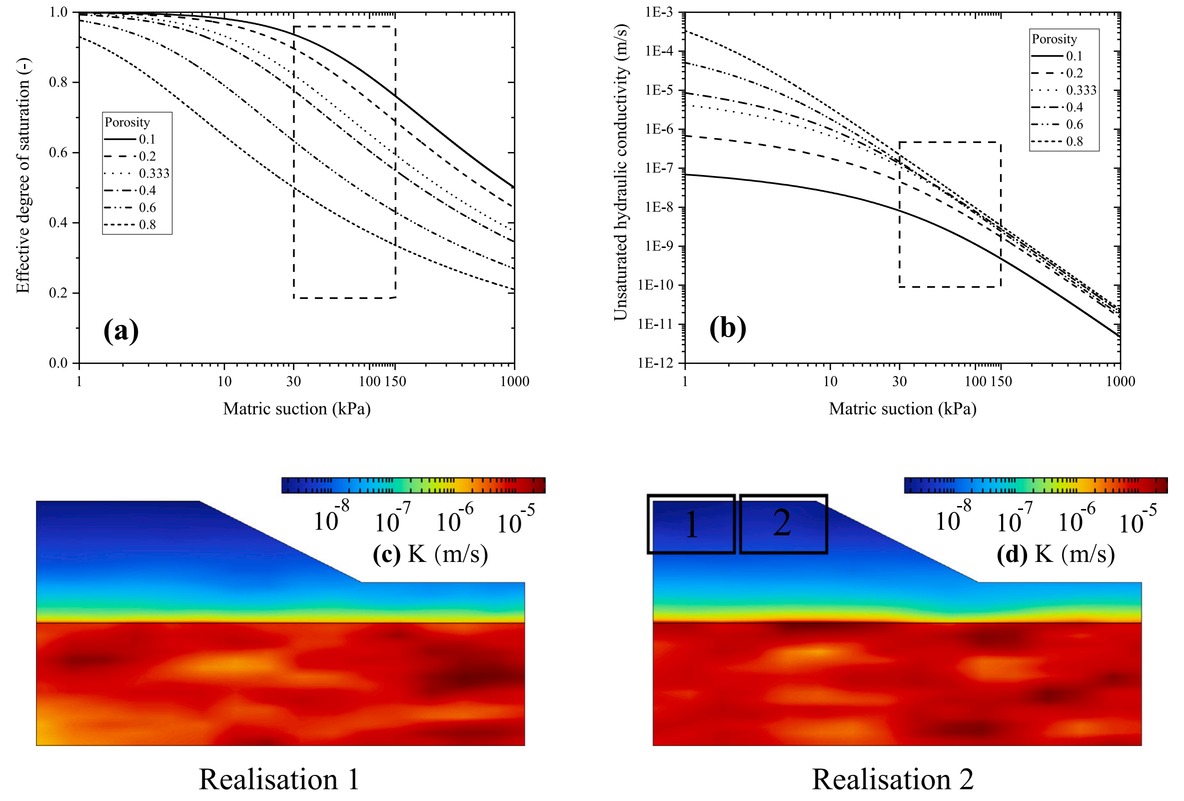

Fig. 7. Relationship between effective degree of saturation and unsaturated hydraulic conductivity with matric suction, initial hydraulic conductivity distribution of two typical realisations: (a) effective degree of saturation versus matric suction; (b) unsaturated hydraulic conductivity versus matric suction; (c–d) initial hydraulic conductivity distribution (zones 1 and 2 are employed to facilitate a comparative analysis of the initial unsaturated hydraulic conductivity).

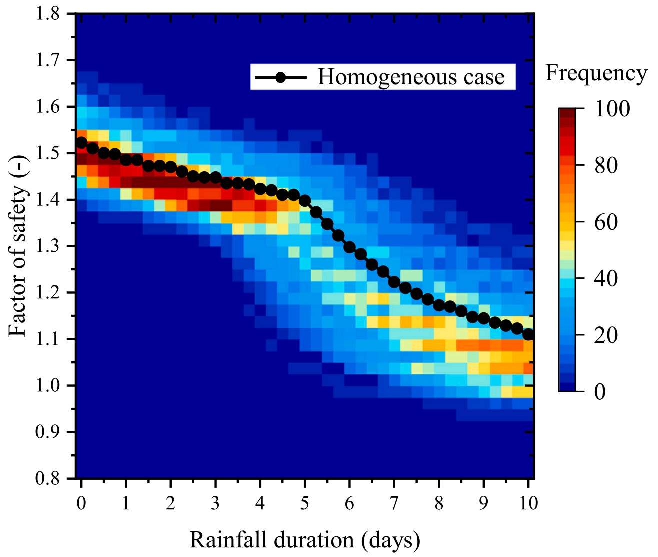

Fig. 8. Heat map of FOS (black dots: homogeneous case). (For interpretation of the references to colour in this figure legend, the reader is referred to the web version of this article.)

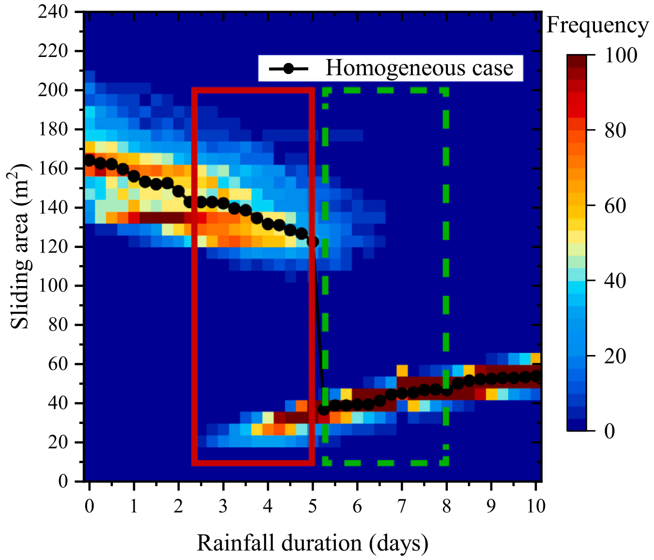

Fig. 9. Heat map of sliding area (m^2) (black dots: homogeneous case; red and green boxes are employed to assess the difference in sliding area between the homogeneous case and heterogeneous cases). (For interpretation of the references to colour in this figure legend, the reader is referred to the web version of this article.)

The deterministic analysis (homogeneous case) in Fig. 9 shows that at the onset of rainfall, there is a deep sliding with a relatively large sliding area (164 m^2), and the sliding area gradually decreases with the rainfall process. After the 5th day, the local areas with low shear strength located between the wetting front and the slope surface are the first to experience sliding failure, with the sliding mechanism of the slope changing from deep sliding to shallow sliding (similar to Fig. 5(c)), causing a decrease in the sliding area from 122 m^2 to 37 m^2. Subsequently, the sliding area gradually increased. During the later stages of rainfall (after the 5th day), the proportion of shallow sliding in the realisations increases, resulting in a relatively narrow distribution of the sliding area and a small standard deviation (e.g., the 'deterministic' PDF of sliding area on the 10th day in Fig. A.23). Throughout most

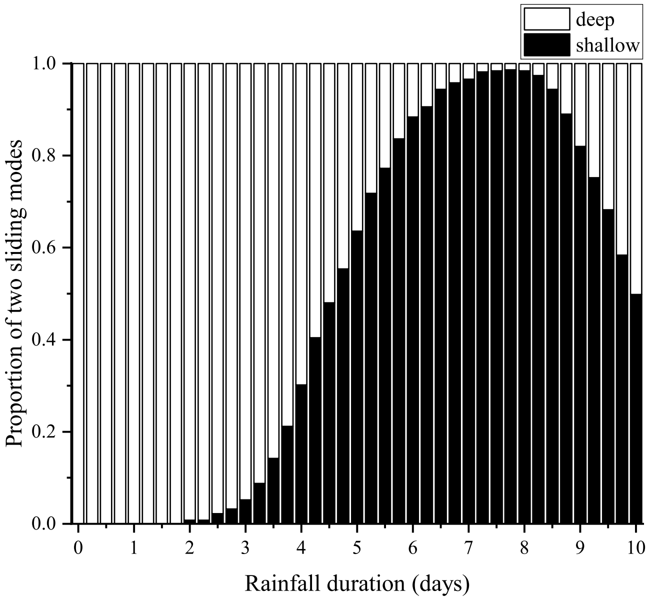

Fig. 10. Proportion of two sliding modes as a function of rainfall duration.

of the rainfall period, the mode of the sliding area obtained from the Monte Carlo simulation was smaller than the sliding area of the homogeneous case. This indicates that simplifying porosity as a constant may overestimate the sliding consequences of the slope, potentially leading to conservative slope protection designs and increased costs.

Simplifying the parameters to constant values gives a single result that may deviate from the actual situation. As shown by the red solid box in Fig. 9, between 2.5 and 5 days of rainfall, some slopes have already taken on shallow sliding (A_s: approximately 20–45 m^2), indicating that shallow sliding is likely to have occurred on the heterogeneous slopes. Conversely, the homogeneous case still takes on a deep sliding mechanism (A_s: 100–190 m^2). Additionally, as shown in the green dashed box in Fig. 9, the slope may still exhibit deep sliding even after 5 days of rainfall. The result from the homogeneous case (shallow sliding) underestimates the sliding consequences and may lead to an unsafe estimate. Inaccurate estimates of sliding consequences could lead to biased risk evaluations.

In order to distinguish the sliding modes implemented throughout the entire rainfall process, the criterion used was the sliding area (55 m^2) of the homogeneous model on the 10th day of rainfall. Realisations with a sliding area less than 55 m^2 were classified as exhibiting shallow sliding, while those with a sliding area greater than 55 m^2 were considered to exhibit deep sliding. Fig. 10 shows that the proportion of two sliding modes progresses over time. The proportion of slopes exhibiting shallow sliding gradually increases after 4 days of rainfall, and by the 5th day, more than half of the slopes exhibit shallow sliding. As rainfall continues, the sliding area increases in some realisations, and some slopes revert to deep sliding during the later stages of rainfall.

In this paper, the transition timing of the sliding mechanisms for the homogeneous case is the 5th day, while for the heterogeneous cases, it may occur as early as 2 days after the start of rainfall. This discrepancy may result in the homogeneous model providing an unrealistic estimate. The size of the sliding area is directly influenced by the sliding mechanism of the slope, which in turn determines the scale of landslide prevention. Analysing the transition timing of the sliding mechanism of the slope is crucial, because the transition of the sliding mechanism affects the scope of emergency responses required for slope management. Additionally, the transition timing of the sliding mechanisms determine when emergency measures need to be implemented. Understanding this transition timing is essential for effective slope management and risk mitigation strategies.

3.5. Groundwater level

If the permeability of the soil around the slope is low or the drainage conditions around the slope are poor (i.e., a no-flow boundary condition along the GH may be appropriate), rainwater may accumulate in the slope, causing a higher rising height of groundwater level. This will further increase the changes in FOS and sliding area. Consequently, the performance of the slope is further investigated when the boundary condition 2 in Table 4 was employed: the no-flow boundary condition was imposed along the GH, while the other hydraulic and mechanical boundary conditions remained unchanged (Section 3.1). Furthermore, the 500 porosity random fields generated in Section 3.1 were still used to characterise the spatial variability of the porosity. On the 10th day of rainfall, the point with the highest pressure head in the homogeneous model is used to represent the groundwater level height, this point is located at (40,0) in boundary condition 1 and (60,0) in boundary condition 2.

Figs. 11(a–c) and 11(e–g) show the variation of groundwater level over time for boundary conditions 1 and 2, respectively. Figs. 11(d) and 11(h) show the arrows pointing to the directions of the flow velocity for realisation 1 on the 10th day of rainfall, with the different colours and/or lengths (of these arrows) representing the magnitudes of the flow velocity. A comparison of these figures reveals that the internal groundwater flow velocity in Fig. 11(h) is significantly higher than in Fig. 11(d), with a maximum of 10 times higher. This high groundwater flow velocity within the slope may weaken the soil structure, leading to the expansion of the sliding surface. Additionally, as shown in Fig. 11(h), the top rainwater has not yet reached the initial groundwater level, and the rise in groundwater level within the slope is caused by the horizontal flow of rainwater near the toe of the slope. As water flows into the slope, it accumulates, increasing pore water pressure, which weakens soil strength and increases the potential for further slope instability. Therefore, enhancing drainage measures, particularly near the toe of the slope, may be an effective strategy to prevent the rise of the internal groundwater level and reduce groundwater flow velocity within the slope. Additionally, the rise in groundwater level has reduced the size of the unsaturated zone, which is more pronounced in Figs. 11(f) and 11(h).

Table 4 shows the FOS, sliding area, rising height of groundwater level, and area of unsaturated zone for different boundary conditions on the 10th day of rainfall. Poor drainage around the slope (boundary condition 2) results in a higher rise in groundwater level, which further reduces the area of the unsaturated zone, accelerating the process of saturation at the toe of the slope. Different boundary conditions have little effect on the advancing of wetting front but have a significantly effect on the rising height of groundwater levels. The soil at the slope toe is completely saturated for realisation 1 under boundary condition 2 (see in Fig. 11(f)), and the weight of the soil further increases, making the slope more unstable. Additionally, for realisation 1, the FOS and sliding area of the model employing boundary condition 2 are smaller than those of boundary condition 1. This is because the disappearance of the matric suction at the slope toe further reduces the slope stability, resulting in more superficial slidings. It can be seen that the drainage conditions around the slope have a significant effect on the slope stability, and the application of drainage measures is conducive to improving the slope stability.

Following the analysis of two typical examples, the results of all realisations were counted. The log-normal distribution was found to be an appropriate fit for the results of the Monte Carlo simulation. Therefore, the normal distribution is used to fit the PDF of the logarithmic values of the groundwater level on the 5th and 10th day (Fig. B.26). Fig. 12 presents the heat map of the logarithmic value of the groundwater level as a function of rainfall duration for different boundary conditions. The upper limits of the local colour bars have been set at 300 and 100 as needed. It can be seen from Fig. B.26 that the rising height of the groundwater level in the homogeneous case is observed to be lower

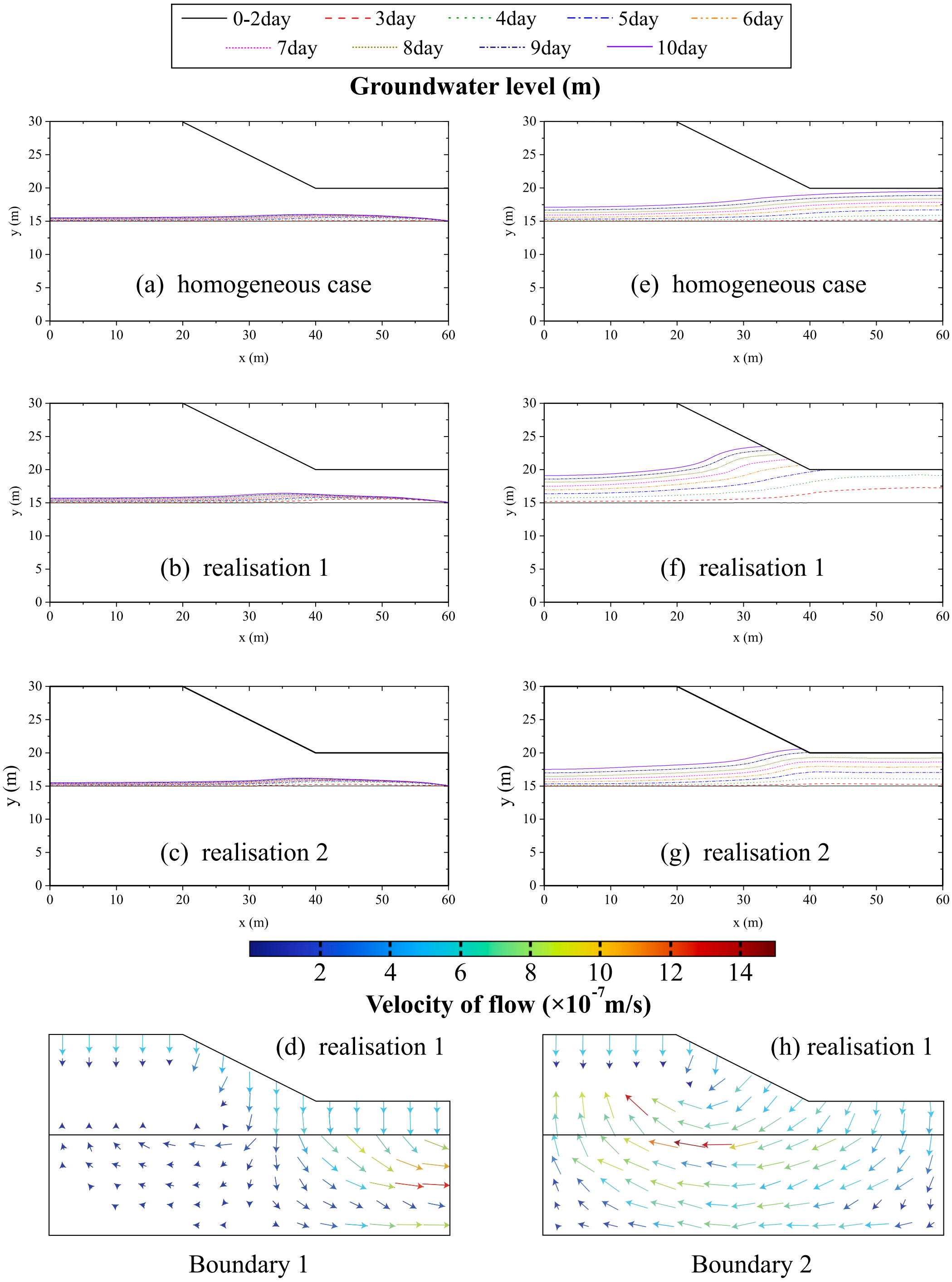

Fig. 11. Changes in groundwater level over time and flow velocity of groundwater on the 10th day: (a–d) boundary condition 1; (e–h) boundary condition 2 (the arrows pointing to the directions of the flow velocity, with the different colours and/or lengths representing the magnitudes of the flow velocity). (For interpretation of the references to colour in this figure legend, the reader is referred to the web version of this article.)

Table 4
Two different boundary conditions of model.

Boundary condition of GH	Case	Rising height of groundwater level (m)	Area of unsaturated zone (m^2)	FOS (-)	Sliding area (m^2)
1	homogeneous	15.69	154	1.12	55
Dirichlet	realisation 1	15.77	143	1.07	54
seepage	realisation 2	15.71	134	1.22	55
2	homogeneous	19.53	111	1.10	52
no-flow	realisation 1	23.62	70	1.02	53
	realisation 2	20.22	79	1.17	38

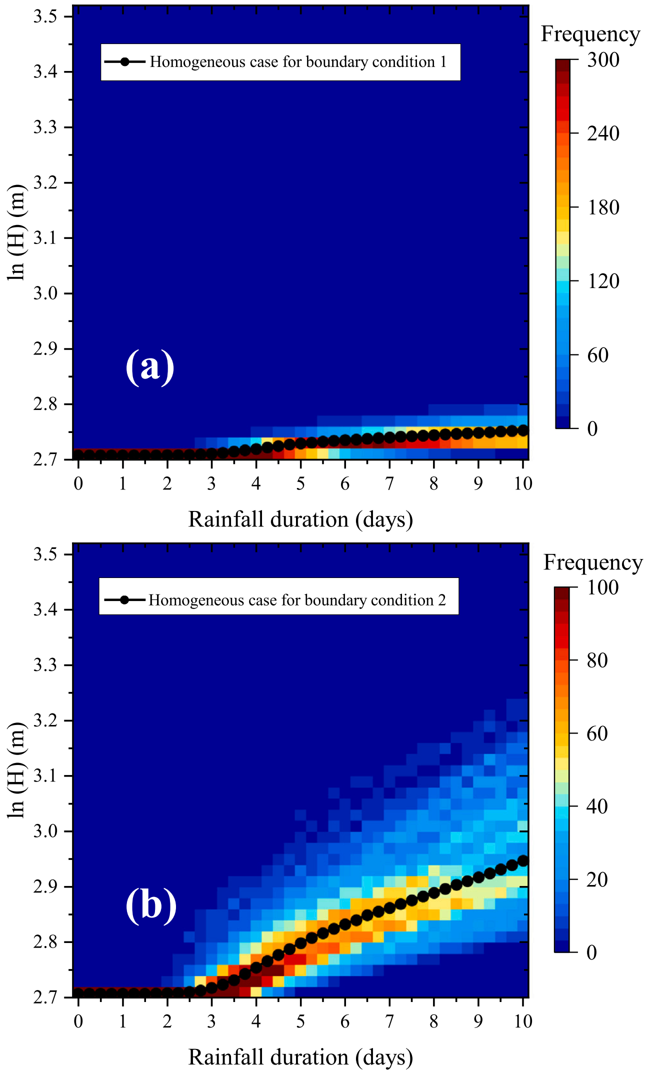

Fig. 12. Heat map of groundwater level for different boundary conditions (black dots: homogeneous case): (a) boundary condition 1; (b) boundary condition 2.

than the mean of the groundwater level in the heterogeneous model. This suggests that the homogeneous case may have underestimated the rising height of the groundwater level, which in turn may have led to an overestimation of the slope stability, which is consistent with the analysis results presented in Section 3.3.

It can be observed that the distribution of groundwater level gradually widens (the COV of groundwater level increases), which is more evident in Fig. 12(b). This indicates that the spatial variability of porosity has a greater influence on the hydraulic response of slopes as rainfall progresses. Simplifying porosity as a constant (and thus making the hydraulic parameters constant) may not accurately reflect reality.

To further investigate the effect of groundwater level changes on the stability of unsaturated slopes, Fig. 13(a) illustrates 10 random realisations, including two typical realisations in Fig. 4. The non-uniform infiltration of rainwater results in different rising heights of groundwater level (different examples have different horizontal coordinates). As shown in Fig. 13(a), the FOS shows a continuous decrease with increasing groundwater level. Fig. 13(b) shows the relationship between the FOS and groundwater level for each time step of all realisations (500 random realisations with 40 time steps per realisation). A correlation analysis was performed on the FOS and the groundwater level height in Fig. 13(b). The results showed a negative correlation between FOS and groundwater level height, with a Pearson correlation coefficient of −0.750, suggesting that slopes with higher groundwater levels have lower stability. When the model adopts boundary condition 2, the Pearson correlation coefficient between the FOS and the height of the groundwater level is −0.805, indicating a stronger negative correlation. This shows that the rise of the groundwater level is another important factor leading to a decrease in slope stability. Ignoring the rise in groundwater level may lead to an overestimation of the slope stability. Therefore, hydraulic boundary conditions have a significant influence on slope stability.

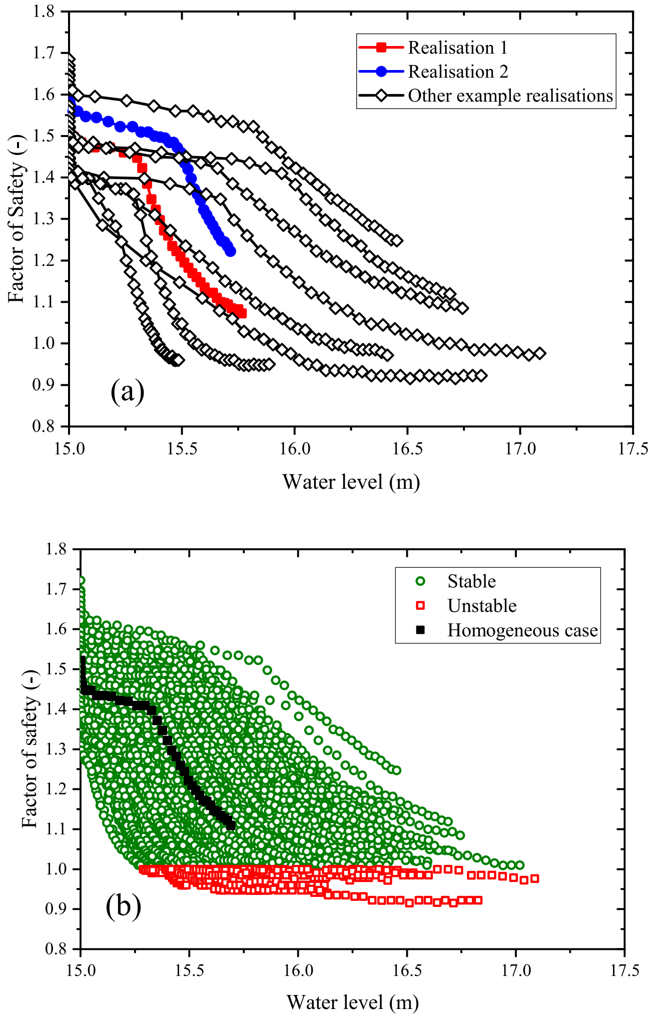

Fig. 13. FOS versus water level (m): (a) 10 random realisations; (b) each time step of all realisations.

The rise in groundwater level reduces the area of unsaturated zones. The combined effect of rising groundwater level and the advancement of the wetting front leads to a reduction in slope stability during rainfall events.

In Fig. 8, the FOS distribution is relatively narrow in the early stages of rainfall, but shows greater variability in the later stages. In contrast, Fig. 9 shows that the sliding area has a greater variability in the early stages of rainfall, while the distribution is relatively narrow in the later stages of rainfall. Comparing Fig. 8 and Fig. 9, it is clear that focusing solely on the FOS or sliding area results in relatively large uncertainties in the slope performance analysis. The risk assessment that combines FOS and sliding consequences can comprehensively consider slope stability and sliding scale and provide new suggestions for designers.

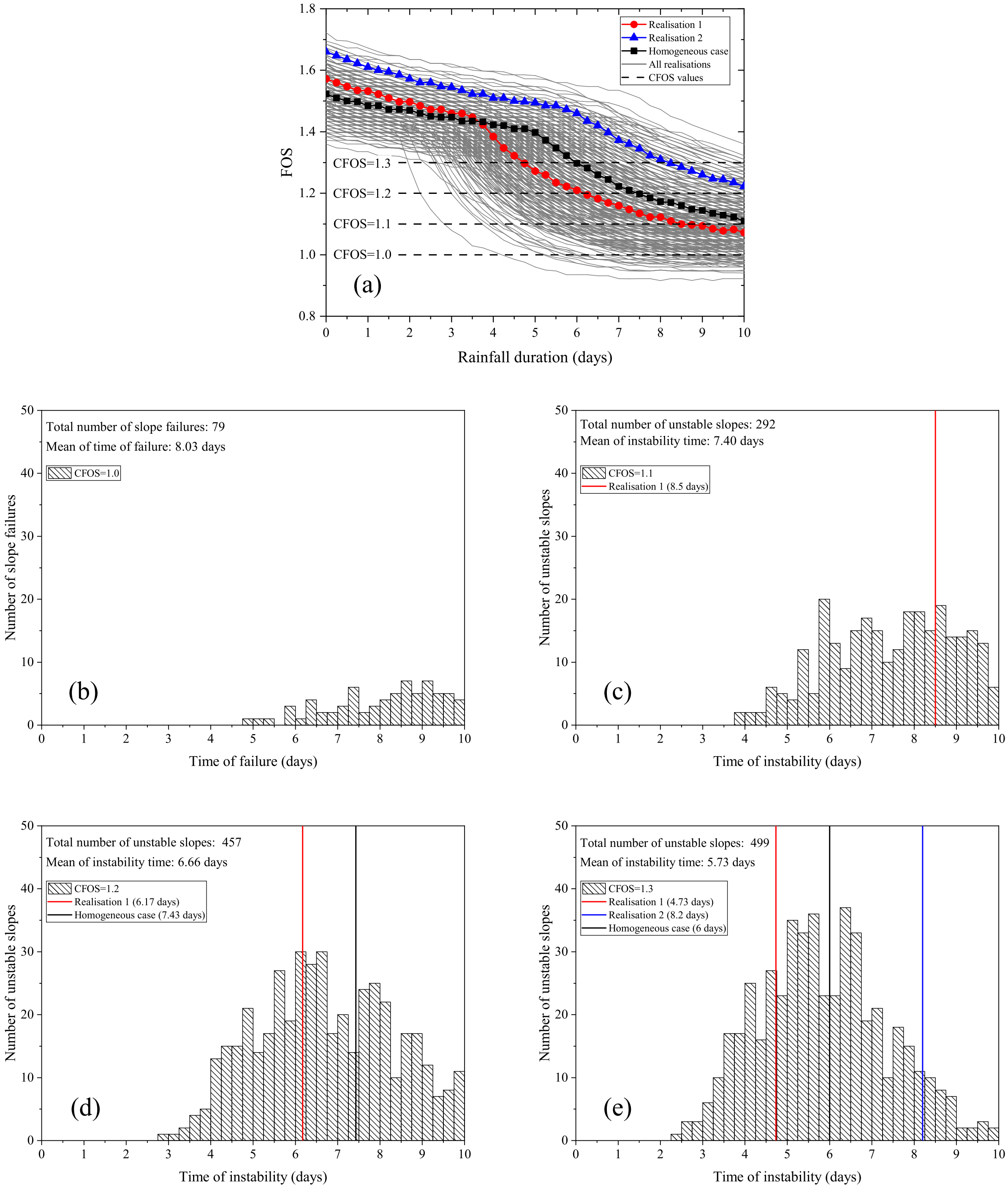

Fig. 14. Temporal FOS and histogram of time of instability/failure for different CFOS: (a) temporal FOS; (b) CFOS = 1.0; (c) CFOS = 1.1; (d) CFOS = 1.2; (e) CFOS = 1.3.

3.6. *Instability/failure time*

The CFOS can serve as a warning threshold for potential landslides. In practical engineering, due to the inherent uncertainties in slope stability analysis (such as variations in soil properties, external loads and simplification in calculation models, etc.), conservative safety criteria may be employed to ensure sufficient safety margins (e.g., CFOS = 1.2–1.3). The model presented in this paper is suitable for slopes with different safety reserve requirements, allowing an appropriate CFOS (warning threshold) to be selected as required.

For a random realisation, the slope is considered unstable if the FOS is less than the CFOS at a given time step, and the time at that point is recorded as the time of instability/failure. Fig. 14(a) shows the temporal FOS for all realisations. Figs. 14(b–e) show the histograms of the time of instability/failure for different CFOS values. In Fig. 14(b), the absence of red, blue, and black vertical lines indicates that even when the rainfall reaches the 10th day, the FOS of the realisation 1, realisation 2 and the homogeneous case remain larger than the CFOS (1.0).

It is evident that the total number of unstable slopes is the largest when CFOS = 1.3. The distribution type of the time of instability is close to a normal distribution when CFOS is large. Additionally, as CFOS increases, the lower limit of the time of instability occurs earlier, resulting in a decrease in the mean time of instability. This suggests that slope failures may occur at earlier stages. For slopes requiring higher safety margins, it is essential to implement early stability monitoring and landslide prevention measures.

Figs. 14(b–e) show that the instability time of the homogeneous case exceeds the mean instability time of the random analysis. In Fig. 14(e), the mean instability time is 5.73 days, indicating that the heterogeneous slopes are likely to become unstable around this time, while the instability time of the homogeneous model is 6 days after the onset of rainfall. The instability time predicted by the homogeneous model may be later than the actual situation, potentially resulting in missed opportunities to implement emergency measures. Additionally, it can be seen from Fig. 14(e) that the instability time of heterogeneous models may occur as early as 2.25 days after the start of rainfall, which is much earlier than the results given by the homogeneous model.

Therefore, it is important to analyse the time of instability/failure of heterogeneous slopes to provide information for early warning of landslides, as well as to determine the appropriate timing for emergency measures (e.g., drainage measures for slopes, support of slopes, and evacuation of people in landslide hazard areas).

3.7. Probability of failure and risk

Fig. 15 shows the FOS and sliding area of the slope on the 0th, 1st, 5th and 10th day. Areas with high FOS and low sliding area are classified as low risk level areas, while areas with low FOS and high sliding area are classified as high risk level areas.

According to the China National Standards (DL/T5353-2006), the FOS of different types of slopes (Class A and Class B) must not be less than 1.20 under transient conditions (rainfall in this paper). Consequently, the critical value of FOS = 1.2 has been chosen as applicable to all types of slopes. Arnold (2016) measured the volume of shallow landslides subject to rainfall in Hong Kong, and found that the sliding volume of a large landslide is greater than 50 m^3. For the 2D model in this paper, the sliding area of 50 m^2 is chosen as the critical value (50 m^3 divided by a unit width of 1 m). Fig. 15 is divided into four quadrants by critical values of FOS and sliding area.

Observation along arrow 1 shows that both the FOS and sliding area gradually decrease from day 0 to day 10, with the risk level of the slope increasing from medium to high. The sliding mechanism in some random realisations changes from deep sliding to shallow sliding on the 5th day. On the other hand, when moving in the direction indicated by arrow 2, the FOS of these realisations (taking on shallow sliding on the 5th day) continues to decrease, while the sliding area increases. This change increases the risk level of the slope from low-medium to high.

Fig. 15 shows that there is a correlation between the FOS and the sliding area. On the 5th day, when the FOS < 1.3, the sliding consequences may be small (20–40 m^2) or large (100–180 m^2). Furthermore, the FOS can be small or large even for slopes with the same sliding consequences. Assessing the performance of a slope based solely on FOS or sliding consequences can be challenging. However, a risk assessment that considers both the FOS and the sliding consequences will compensate for this shortcoming.

The probability and risk of slope instability/failure are calculated using Eqs. (13) and (15), as shown in Fig. 16. The probability and risk of slope instability are low in the early stages of rainfall, and both increase as the rainfall continues.

It is important to note that when utilising CFOS values of 1.1, 1.2 or 1.3, the goal is not to calculate the actual probability of failure and associated risk, but rather to assess the performance of slopes in a more conservative scenario. For instance, in engineering practice, if a slope is located near sensitive areas such as schools, hospitals or residential zones, it may be desirable to evaluate the probability of failure and risk of the slope at CFOS = 1.1 to account for unforeseen contingencies, such as heavy rains or earthquakes. Conversely, medium or low CFOS values suffice for the design of less critical slopes. Therefore, adopting a higher CFOS serves as a method of assessing the failure risk of slopes under more stringent criteria. As illustrated in Fig. 16, as the CFOS increases, the probability of slope failure and risk also increase, this is because greater safety margins are reserved. The appropriate CFOS for a slope must be determined based on the local natural conditions (e.g., the frequency of heavy rainfall or earthquakes), the potential consequences of failure, uncertainties in the surveyed parameters and the numerical models.

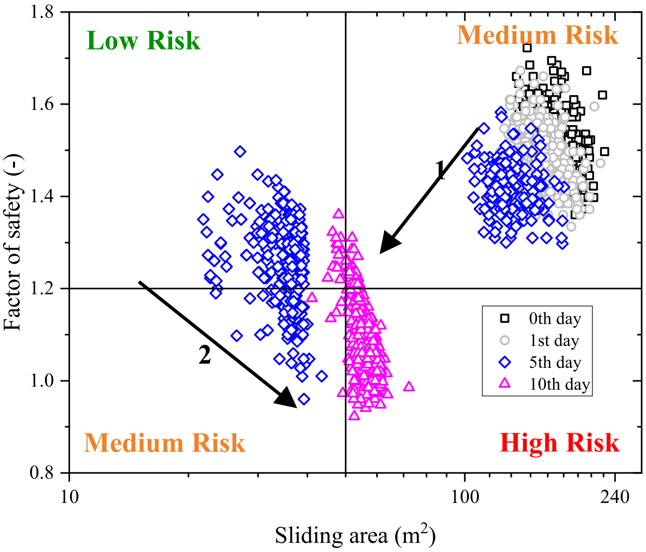

Fig. 15. FOS and sliding area on the 0th, 1st, 5th, 10th day.

Furthermore, as illustrated in Fig. 16(a), the probability of slope instability on the 5th day is 45% when CFOS=1.3. This information is of limited use to designers without additional context (e.g., the level of landslide protection). Moreover, according to Fig. 15, 55% of the slopes are in middle–high risk areas on the 5th day, which can assist designers in implementing landslide protection measures or issuing early warnings based on the risk level of the slope.

The CFOS = 1.3 curve in Fig. 16(a) shows that the probability of slope instability exceeds 90% within 8–10 days of rainfall, after which the curve flattens. In contrast, the CFOS = 1.3 curve continues to rise in Fig. 16(b). This comparison suggests that, as the slope approaches instability, the increase in instability probability is not as steep as the increase in risk. It indicates that the cumulative effect of risk is more significant than that of instability probability. The cumulative effect implies that even if the probability of instability does not rise sharply in the short term, the increasing potential losses demand enhanced preventive measures. This emphasises the need for decision-makers to focus more on changes in risk as the slope nears failure. Furthermore, risk analysis can provide better support for decision-makers in evaluating the scale of emergency measures, enabling more effective cost–benefit analyses.

In practice, combining both qualitative and quantitative risk assessments of slopes, which consider both the FOS and the sliding consequences, can offer comprehensive information and guidance to decision-makers. This is essential to ensure the safety of individuals residing in the affected areas.

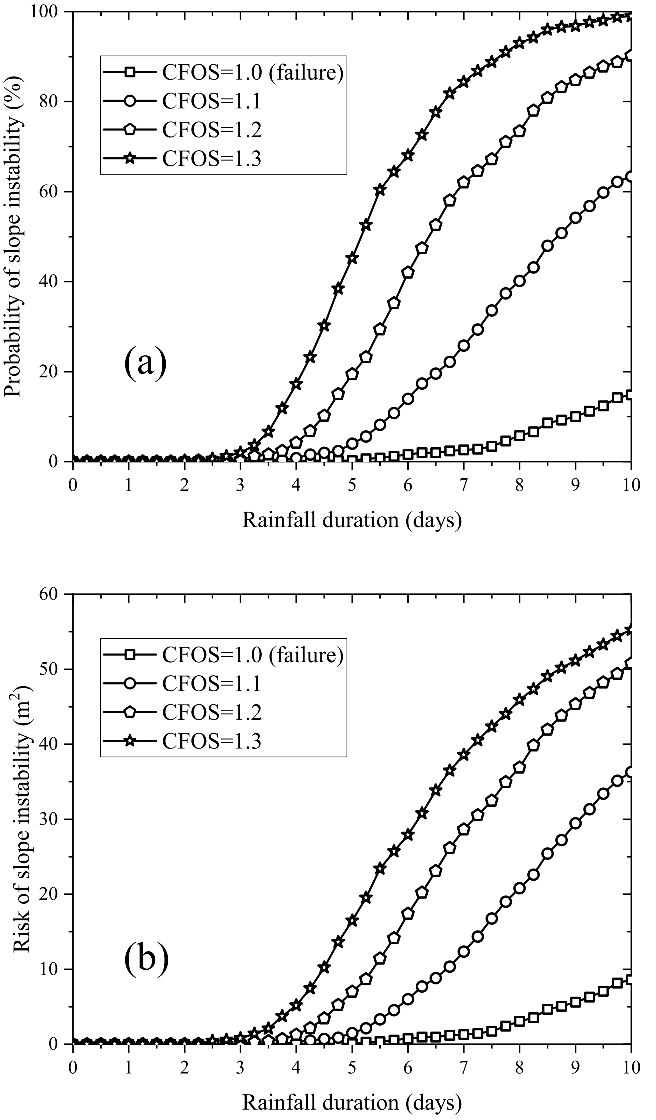

Fig. 16. Probability of slope instability/failure and risk: (a) probability of slope instability/failure; (b) risk (m^2).

4. Illustrative example 2: Malin slope

The Malin slope, located in the Malin village (Geographical coordinates: Latitude N19 ° 09' 41.4", Longitude E73 ° 41' 16.8"), Ambegaon Tehsil of Pune District in western Maharashtra, India, experienced a sliding failure on July 30, 2014 following a continuous heavy rainfall event. The slope was divided into four zones, designated as Zone 1 through Zone 4. Pan et al. (2024) conducted an inverse analysis of soil parameters of the Malin slope to predict changes in slope reliability over time. Due to limited data availability, the temporal stability and risk of the Malin slope are investigated to verify the effectiveness of the framework proposed in this paper.

4.1. Slope model and characterisation of the spatial variability of soil parameters

According to Pan et al. (2024), the potential instability zone (Zone 3) of the Malin slope is selected to establish the finite element model. The boundary conditions and finite element mesh are depicted in Fig. 17. A fixed total water head boundary is applied with an upstream water level of 20 m and a downstream water level of 10 m. The slope surface (CDEF) is assigned as the rainfall boundary condition, and BC and FG are assigned as the impermeable boundaries. COMSOL Multiphysics offers a user-defined option in the Richards' equation, allowing the user to input custom equations for defining the SWCC and relative hydraulic conductivity. In this section, the FX model and the Leong and Rahardjo model (Pan et al., 2024) were utilised to represent the hydraulic properties of the soil.

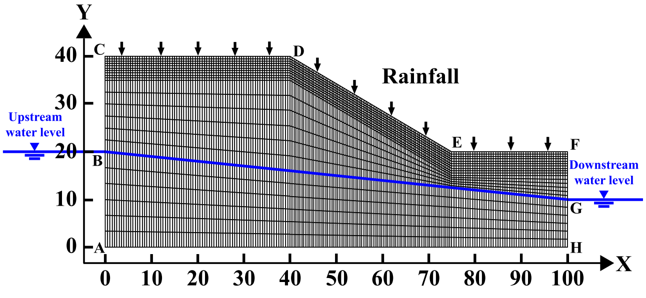

Fig. 17. Finite element model and boundary conditions of the Malin slope.

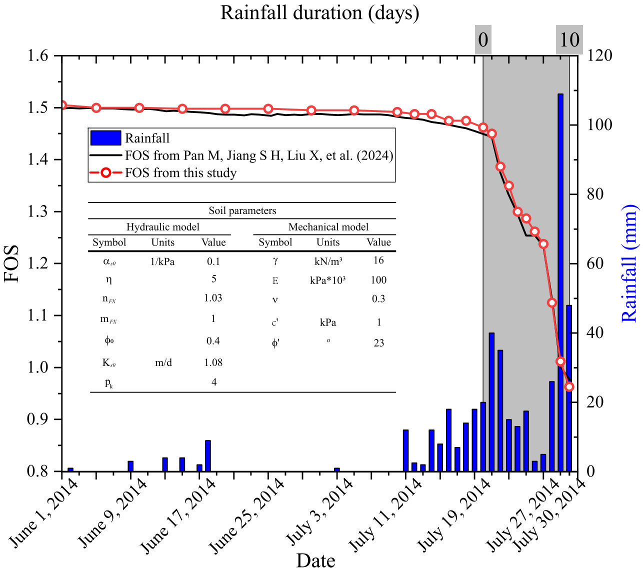

Soil parameters

Hydraulic model			Mechanical model		
Symbol	Units	Value	Symbol	Units	Value
α_{s0}	1/kPa	0.1	γ	kN/m³	16
η		5	E	kPa*10³	100
n_{FX}		1.03	ν		0.3
m_{FX}		1	c'	kPa	1
ϕ_0		0.4	ϕ'	°	23
K_{s0}	m/d	1.08			
p_k		4			

Fig. 18. Table of parameters and comparison of FOS obtained from the current study and Pan et al. (2024) (the grey box highlights the time periods that are the focus of this study).

Given that the Malin slope ultimately failed due to shallow sliding, a smaller finite element cell size is used for the shallow surface layer, while a larger finite element cell size is used for the rest of the slope to improve computational efficiency. The chosen finite element cell sizes were demonstrated to meet the accuracy requirements (see Fig. 18 for deterministic model calculations). In addition, the sliding area (July 30, 2014) of the homogeneous model calculated by the spectral clustering method, differed by less than 1% from the results reported in Pan et al. (2024). This paper focuses on the performance of the Malin slope over a 10-day period from July 20, 2014 to July 30, 2014. The rainfall duration in subsequent sections is expressed as ranging from 0 to 10 days.

Ering et al. (2015) and Singh et al. (2016) reported that no field investigation data were collected prior to the Malin slope failure, and only a limited number of representative or disturbed soil samples were obtained from three locations at the base, middle, and top of the slope after the Malin slope failure. Therefore, as shown in Fig. 18, the soil parameters used in this paper are consistent with those in the study of Pan et al. (2024). The mean porosity adopted in this study is 0.4, with a COV of 0.2, a vertical SOF of 3 m and a horizontal SOF of 30 m.

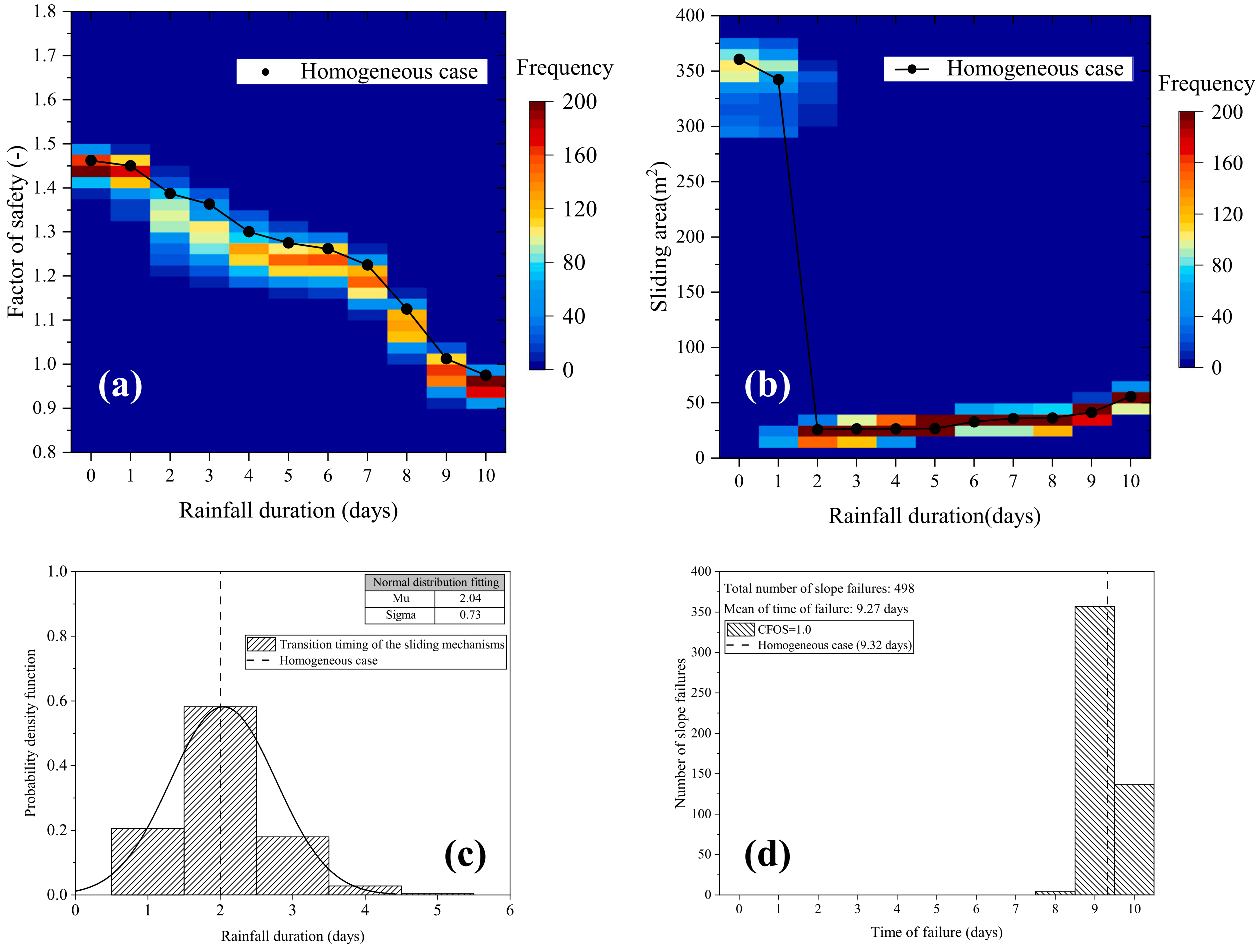

Fig. 19. (a–b) Heat map of FOS and sliding area for the Malin slope (black dots: homogeneous case); (c) PDF of transition timing of sliding mechanisms for the Malin slope (dashed line: homogeneous case); (d) Histogram of time of failure for the Malin slope (dashed line: homogeneous case).

4.2. Temporal stability and risk analysis of malin slope

As illustrated in Fig. 19(a), the FOS for the homogeneous case is generally larger than the mode of the FOS derived from the Monte Carlo simulations. This suggests that the homogeneous case may have overestimated the stability of the Malin slope. The variability in FOS is more pronounced in the middle of the rainfall period (within 1–5 days) and smaller at the early and later stages (0–1 and 5–10 days), which is consistent with the analysis presented in Section 3.3. This phenomenon is attributed to changes in the sliding mechanism of the heterogeneous slopes within 1–5 days, which further accelerates the decrease in the FOS. Continuous rainfall over 7–10 days leads to a further reduction in the matric suction of the shallow soil, which accounts for the additional decrease in FOS during the later stages of rainfall. Fig. 19(b) indicates that the sliding mechanism of some slopes changes as early as the 1st day of rainfall. Additionally, Fig. 19(c) shows the PDF of transition timing of the sliding mechanism for all realisations. The results show that the probability density function value reaches its maximum on the 2nd day, indicating that the sliding mechanism of the Malin slope is most likely to change on this day. However, due to the presence of spatial variability in soil properties, the transition timing of the Malin slope sliding mechanism may be advanced to the 1st day or delayed until the 5th day. It is important to note that the Malin landslide was not predicted in advance, and therefore there is insufficient field investigation data to directly confirm the actual transition timing of the Malin slope sliding mechanism.

Fig. 19(d) shows the distribution of failure times for the heterogeneous Malin slope, with a mean failure time of 9.27 days. This suggests that the Malin slope is most likely to fail after the 9th day (i.e., on the 10th day), which is consistent with the observations from the actual site. It proves the effectiveness of the framework proposed in this paper. In addition, the failure time for the homogeneous Malin slope is 9.32 days, which is later than that the mean of failure time for the heterogeneous Malin slopes. This indicates that neglecting the spatial variability of soil parameters may lead to an unsafe estimation of slope failure time. These findings are consistent with the analysis presented in Section 3.6.

The change in risk level of the heterogeneous Malin slope can be represented by connecting the FOS-sliding area coordinate points at each time step, as shown in Fig. 20, using the FOS = 1.0 and the sliding area = 56 m^2 (the deterministic sliding area on the 10th day) as the critical thresholds. Initially, the Malin slope is at a medium risk level. As rainfall persists, the sliding mechanism of the Malin slope changes, leading to a sudden reduction in the sliding area, which lowers the risk to a low level. However, with continued rainfall, the stability of the Malin slope decreases sharply and the sliding area further increased, ultimately raising the slope to a high sliding risk level. It is important to note that the risk level reflects the potential impact if the slope fails in its current state. For instance, on the 2nd day, the homogeneous Malin

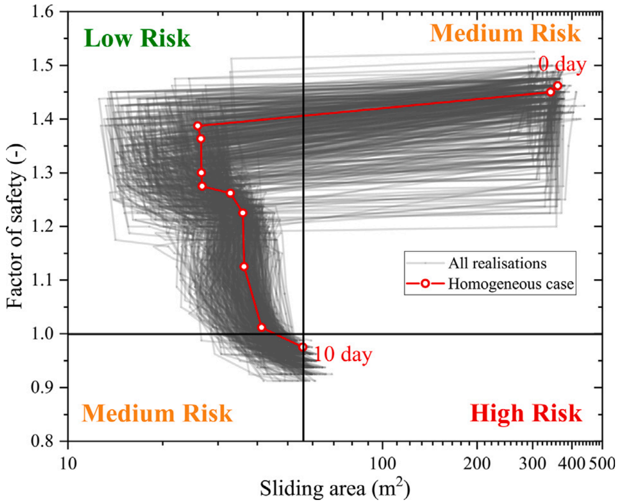

Fig. 20. Quadrant figure of the risk of the Malin slope.

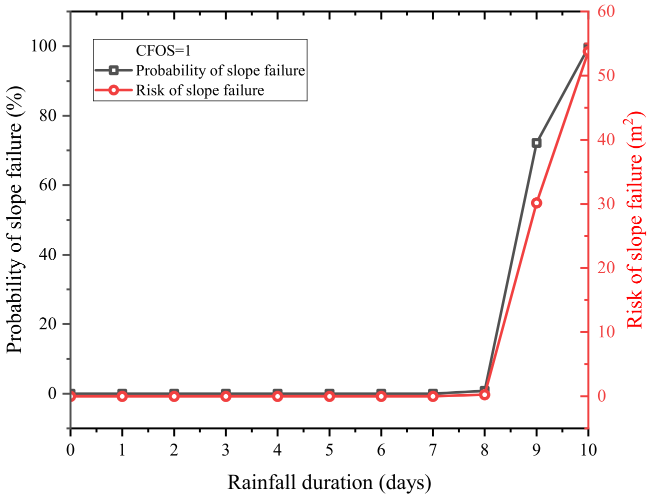

Fig. 21. Probability of failure and risk of Malin slope.

slope has an FOS of 1.39, indicating a low likelihood of failure. Even if failure occurs, the sliding area is only 26 m^2, placing the slope at a low risk level.

Fig. 21 presents a statistical representation of the failure probability and risk at the critical state of the Malin slope. It can be observed that both failure probability and risk increase sharply on the 9th and 10th days. This indicates that not only is the failure probability increasing, but the consequences of slope failure are becoming increasingly severe. Once the heavy rainfall on the 9th day ceases, failure of the Malin slope is almost inevitable. Additionally, the increase in risk between the 9th and 10th days remains significant, indicating that the potential harm caused by slope failure continues to rise. Increased risk demands more attention and intervention than failure probability, as it signifies the need for a more timely and robust response measures.

5. Conclusion

This study simultaneously considers the impact of spatial variability in porosity on matric suction and shear strength parameters, and ultimately its effect on the probability of instability/failure and risk of unsaturated slopes subject to rainfall. The RFEM is adopted to evaluate the advancing of the wetting front, the height of the groundwater level and the distribution of the effective degree of saturation. The stability of slopes is investigated by SRM, and spectral clustering method is used to obtained the sliding area. Subsequently, the time of instability/failure, probability of failure and risk of slope failure are quantified. Finally, a real Malin slope is investigated to demonstrate the effectiveness of the proposed approach. The key conclusions of the present study are as follows:

(1) The spatial distribution of porosity and unsaturated hydraulic conductivity jointly affect the advancing speed of wetting front. In the unsaturated zone, less variation in unsaturated hydraulic conductivity for different porosity values. Over the same rainfall duration, zones with lower porosity experience a greater proportion of soil with changes in initial effective saturation, resulting in the wetting front advancing more rapidly in these areas. Therefore, in this study, the spatial distribution of porosity is the primary factor, while unsaturated hydraulic conductivity is the secondary factor. It is reasonable to set porosity as the fundamental parameter to represent the spatial variability of soil. If only the spatial variability of saturated hydraulic conductivity were considered, with porosity assumed to be constant, the opposite conclusion may be obtained.

(2) During the “relatively small” rainfall event, the sliding mechanism of the slope changes from deep sliding to shallow sliding. This transition is influenced by the advancing of wetting front and can cause a sudden decrease in FOS. The transition timing of sliding mechanisms for the homogeneous case is the 5th day, while for heterogeneous cases, it may occur as early as 2 days after the start of rainfall. After 5 days of rainfall, the heterogeneous slope may still exhibit deep sliding (although the proportion is small), while the result of the homogeneous model is shallow sliding that may underestimate the sliding consequences and lead to an unsafe estimation. In the later stages of rainfall, some slopes take on deep sliding again. In the long term after the end of the rainfall, the proportion of slopes take on deep slip will continue to increase. The change in sliding area is related to the transition of the sliding mechanism, and the timing of the transition of sliding mechanism is critical in determining the scope and timing of a reasonable emergency response.

(3) The impacts of two different hydraulic boundary conditions on slopes were studied. The source of the rise in the groundwater level on the left side of the slope is the horizontal flow of rainfall water around the slope toe area, rainfall water at the top of the slope does not flow to the initial groundwater table. The homogeneous case may underestimate the rising height of groundwater level and therefore may overestimate the slope stability. The rising height of groundwater level is negatively correlated with FOS with a correlation coefficient of −0.750, which is more obvious when the model adopts a no-flow boundary condition (correlation coefficient is −0.805). The advancing of the wetting front and the rising of groundwater level jointly drive slope failure, therefore the horizontal (or near the toe of the slope) drainage conditions are important to consider in realistic cases.

(4) Analyses of both the typical embankment slope and the Malin slope suggest that the homogeneous case may overestimate the stability of slopes. When the spatial variability of the internal friction angle is additionally considered, the homogeneous case may significantly overestimate slope stability. The time of instability/failure may be delayed, potentially resulting in missed opportunities for early warning and the implementation of emergency measures (e.g., evacuation of people in landslide hazard areas). Therefore, incorporating the spatial variability of parameters in slope stability analysis is crucial. Appropriate consideration of spatial variation of parameters based on actual survey results can lead to more accurate prediction of slope instability/failure time.

(5) Risk-based assessment enables the determination of risk levels, and the quadrant figure of the FOS-sliding area shows that the risk level initially decreases and then increases as rainfall progresses. Quantitative analysis indicates that the risk increases as rainfall progresses. Compared to the probability of instability/failure, risk has

a more pronounced cumulative impact. Therefore, greater attention should be directed towards changes in risk as the slope approaches failure. In addition, when the spatial variability of the internal friction angle is additionally considered, the overall level of probability of instability/failure and risk will increase.

Additionally, it is important to note that real engineering scenarios are often more complex, and obtaining accurate parameters presents significant challenges. The accuracy of the framework proposed in this study is highly dependent on both the precision of the parameters and the model. While this study has achieved certain results, there is still room for further development. Future research will focus on reducing the uncertainties in hydraulic and mechanical parameters. For example: (i) the use of conditional random fields is necessary to better represent the spatial distribution of actual site parameters (e.g., Li et al. (2016)); and (ii) data assimilation techniques are needed to further reduce parameter uncertainties (e.g., Liu et al. (2018), Mohsan et al. (2021)). Once a comprehensive database of hydraulic and physical parameters for the actual slope is established, it can be easily incorporated into the model used in this paper. The methods for stability and risk assessment demonstrated in this study are applicable to complex slopes and can be extended to other types of soil.

Notations

CFOS	critical factor of safety
COV	coefficient of variation
FOS	factor of safety
KNN	k-nearest neighbour method
LAS	local average subdivision method
MC	Mohr–Coulomb
Ncut	normalised-cut method
PDF	probability density function
RFEM	random finite element method
SWCC	soil–water characteristic curve
SOF	scale of fluctuation
SRM	strength reduction method
VG	van Genuchten
α_{s0}	base value of $\alpha_{VG/FX}$
α_{VG}	approximately the inverse of the air-entry suction head for main curve of VG model
α_{FX}	approximately the inverse of the air-entry suction head for main curve of FX model
γ	unit weight of the soil
η	the rate at which control parameters deviate from their base values
θ	scale of fluctuation
θ_r	residual volumetric water content
θ_s	saturated volumetric water content
θ_w	volumetric water content
μ	mean
μ_w	viscosity of water
ν	Poisson's ratio
ρ	correlation coefficient between two points
ρ_w	fluid density
σ	standard deviation
σ_t	total stress
τ_f	soil shear strength
ϕ	porosity
ϕ'	effective friction angle
ϕ_0	base value of porosity
ϕ'_{fail}	effective friction angle during failure
χ	effective stress parameter
$\boldsymbol{A}$	similarity graph
A_s	sliding area
C	consequence of failure
C_m	specific moisture capacity
c'	effective cohesion
c'_{fail}	effective cohesion during failure
D_e	elevation
E	Stiffness (Young's modulus)
e	void ratio
e_{eluer}	the Euler's number
g	acceleration of gravity
K	hydraulic conductivity
K_r	relative hydraulic conductivity
K_s	saturated hydraulic conductivity
K_{s0}	base value for K_s
k	constant in Caquot's relationship
k_p	number of eigenvectors of Laplacian matrix
m_{FX}	fitting parameter for the soil–water characteristic curve of FX model
m_{VG}	fitting parameter for the soil–water characteristic curve of VG model
n_{FX}	fitting parameter for the soil–water characteristic curve of FX model
n_{VG}	fitting parameter for the soil–water characteristic curve of VG model
n_f	number of failure cases
n_{real}	number of realisations
p	water pore pressure
p_f	probability of failure
p_k	the constant related to the soil type
Q_m	fluid source (positive) or sink (negative)
q	rainfall infiltration rate
R	risk
S	water storage coefficient
S_e	effective degree of saturation
t	time
u	the fluid velocity
u_a	pore air pressure
u_w	pore water pressure
∇	gradient operator

CRediT authorship contribution statement

Cheng Qian: Writing – original draft, Visualization, Validation, Software, Methodology, Investigation, Formal analysis. **Yajun Li:** Writing – review & editing, Supervision, Resources, Project administration, Methodology, Investigation, Funding acquisition, Data curation, Conceptualization. **Philip J. Vardon:** Writing – review & editing, Validation, Software, Methodology. **Wei Shao:** Writing – review & editing, Software, Methodology, Data curation. **Jiahe Song:** Writing – original draft, Visualization, Methodology, Investigation, Formal analysis, Data curation. **Bin Zhang:** Writing – review & editing, Supervision, Software, Methodology. **Nengxiong Xu:** Writing – review & editing, Supervision, Software, Methodology.

Declaration of competing interest

The authors declare that they have no known competing financial interests or personal relationships that could have appeared to influence the work reported in this paper.

Acknowledgements

The first author appreciates the financial support of the National Natural Science Foundation of China (grant no. 41807228).

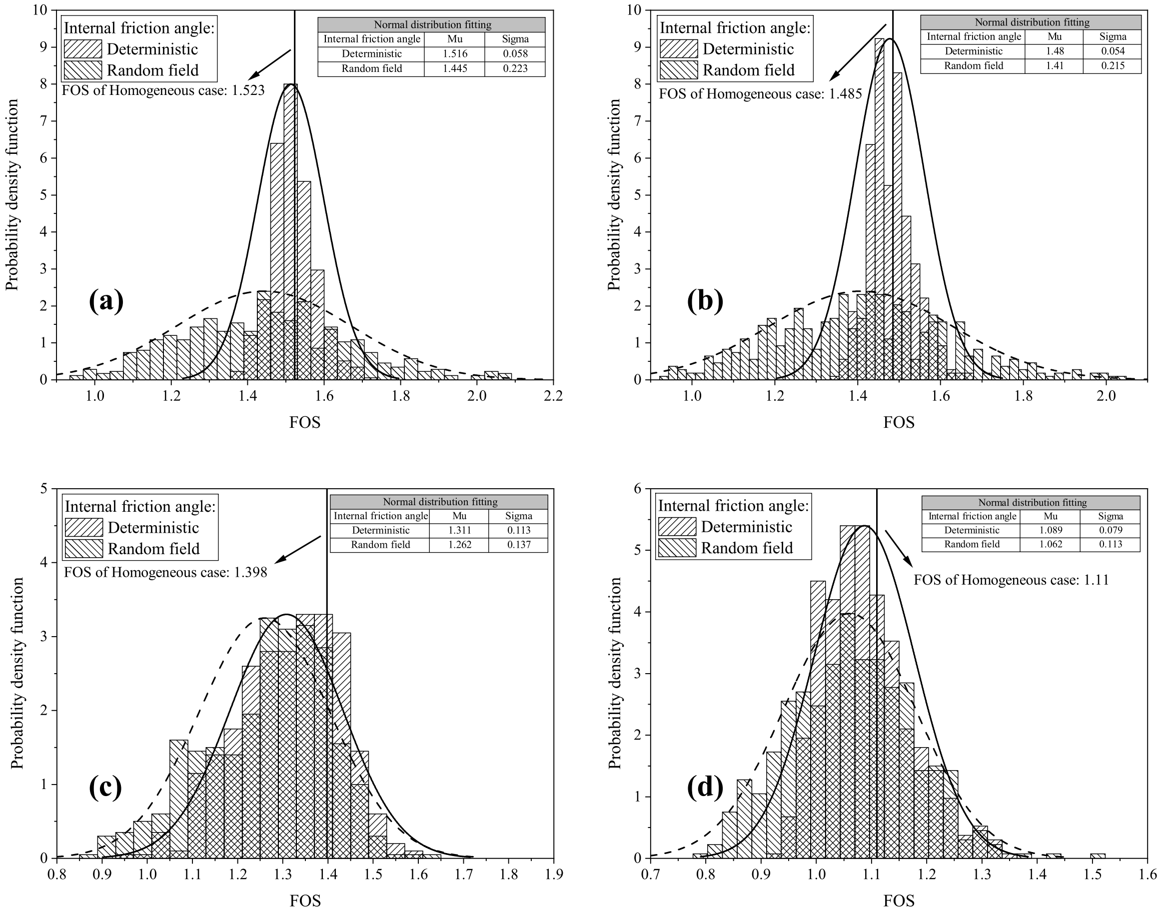

(a)

Normal distribution fitting		
Internal friction angle	Mu	Sigma
Deterministic	1.516	0.058
Random field	1.445	0.223

(b)

Normal distribution fitting		
Internal friction angle	Mu	Sigma
Deterministic	1.48	0.054
Random field	1.41	0.215

(c)

Normal distribution fitting		
Internal friction angle	Mu	Sigma
Deterministic	1.311	0.113
Random field	1.262	0.137

(d)

Normal distribution fitting		
Internal friction angle	Mu	Sigma
Deterministic	1.089	0.079
Random field	1.062	0.113

Fig. A.22. PDFs of FOS: (a) the 0th day; (b) the 1st day; (c) the 5th day; (d) the 10th day (Mu and Sigma: mean value and standard deviation for FOS).

Appendix A. Effect of spatial variability of internal friction angle on slope performance

In this section, both the spatial variability of hydraulic parameters and the internal friction angle are considered. The internal friction angle is related to the void ratio by Caquot's relationship (Mouyeaux et al., 2018), as expressed in Eq. (A.1), where k represents a constant. Therefore, once the spatial variability of the void ratio is determined, the spatial variability of the internal friction angle can be characterised accordingly.

$$e \cdot \tan(\phi) = k \tag{A.1}$$

The k value used in Eq. (A.1) is 0.1376, this value is obtained by the back-figured average void ratio and the deterministic value of the internal friction angle (see in Table 1).

The PDFs of the FOS and sliding area on the 0th, 1st, 5th and 10th day of rainfall are shown in Figs. A.22 and A.23. These figures contain two scenarios for setting the internal friction angle: constant value and random fields. As shown in the figures, the statistical trends are generally consistent across both scenarios. For example, Fig. A.22(a) illustrates that the homogeneous case may overestimate the slope stability, and this observation remains valid whether the internal friction angle is treated as a constant or as a random field.

Fig. A.24 shows the quadrant figure of the FOS-sliding area, where most realisations are at medium risk levels, with some at high risk levels on days 0 and 1 of rainfall. Most realisations are at high risk levels on the 10th day of rainfall. The trend in risk level changes is consistent with Fig. 15. The probability of slope instability/failure and risk under different CFOS are shown in Fig. A.25. It can be observed that both the probability of slope instability/failure and risk generally increase as rainfall progresses. Using the curve with CFOS = 1.3 as an example, the probability of instability increases more slowly in the later stages of rainfall, while the risk continues to show an upward trend, with trends consistent with Fig. 16.

However, comparing the results of setting the internal friction angle as random field and deterministic value, additional information can be found. The variability of the PDFs for the FOS and sliding area is greater when the internal friction angle is modelled as a random field, as the spatial variability introduces uncertainty into the slope system. As shown in Fig. A.22, the mean FOS obtained from the Monte Carlo simulation is consistently lower when the internal friction angle is modelled as a random field compared to the deterministic value. This suggests that ignoring the spatial variability of the internal friction angle may lead to a significant overestimation of slope stability. Similarly, Fig. A.23 shows that the mean sliding area obtained from the Monte Carlo simulation is consistently larger when the internal friction angle is set as a random field. This indicates that neglecting the spatial variability of the internal friction angle may lead to a significant underestimation of the sliding area.

The combined analysis of Figs. A.22 and A.23 suggests that setting the internal friction angle as a constant may underestimate the probability of instability/failure and risk of slope, as demonstrated

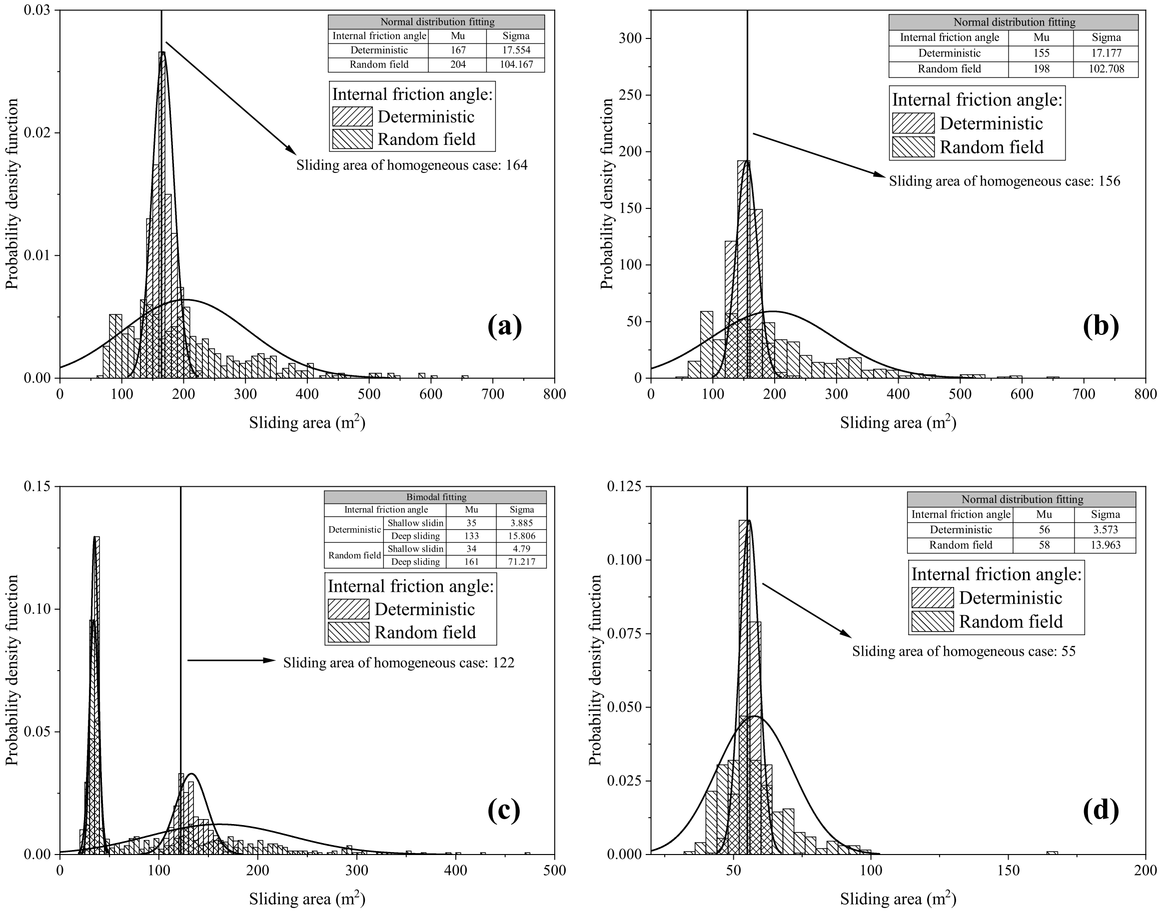

Fig. A.23. PDFs of sliding area: (a) the 0th day; (b) the 1st day; (c) the 5th day; (d) the 10th day (Mu and Sigma: mean value and standard deviation for sliding area).

in Figs. A.24 and A.25. In Fig. A.24, it is evident that on day 0 of rainfall, some realisations already exhibit high-risk levels, whereas in Fig. 15, all realisations are classified as medium risk level. Fig. A.25 further confirms this conclusion: when the spatial variability of the internal friction angle is considered, the probability and risk of failure are greater than zero on day 0 of rainfall. For CFOS = 1.3, the failure probability reaches 26.8%, and the risk increases to 40 m^2, whereas in Fig. 16, both the failure probability and risk on day 0 are zero. This further emphasises that setting the internal friction angle to a constant value may underestimate both the probability and risk of slope failure.

The FOS and sliding area are highly sensitive to the internal friction angle. When the spatial variability of the internal friction angle is considered, the COV of the FOS and the sliding area will increase, further affecting the values of instability/failure probability and risk. However, this does not alter the overall trends in the development of instability/failure probability and risk.

Appendix B. PDF of water level

Fig. B.26 shows the PDFs of logarithm value of the groundwater level on the 5th, 10th day.

Data availability

Data will be made available on request.

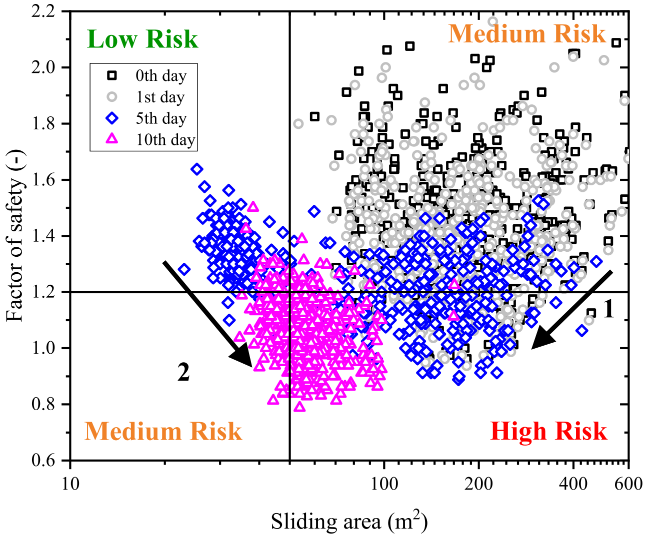

Fig. A.24. FOS and sliding area on the 0th, 1st, 5th, 10th day (considering the spatial variability of internal friction angle).

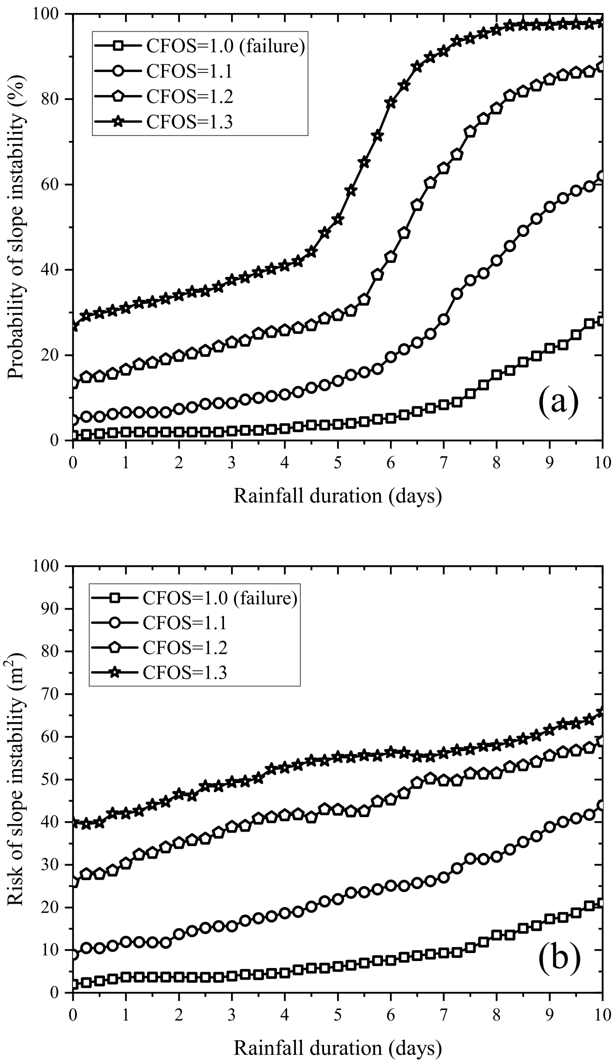

Fig. A.25. Probability of slope instability and risk (considering the spatial variability of internal friction angle): (a) probability of slope instability/failure; (b) risk (m^2).

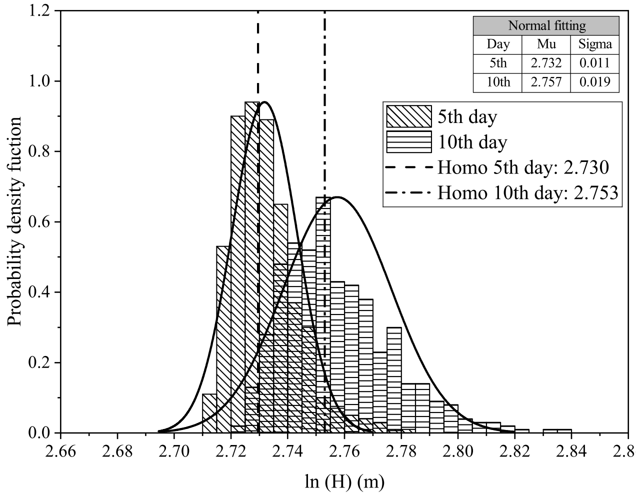

Fig. B.26. PDFs of logarithm value of the groundwater level (Homo: homogeneous case; Mu and Sigma: mean value and standard deviation for logarithm value of the groundwater level).

References

Arnold, P., 2016. Probabilistic Modelling of Unsaturated Slope Stability Accounting for Heterogeneity (Ph.D. thesis). The University of Manchester (UK).

Arnold, P., Hicks, M.A., 2011. A stochastic approach to rainfall-induced slope failure. In: Third International Symposium on Geotechnical Safety and Risk. ISGSR. Munich, Germany, Bundesanstalt FÜR Wasserbau, Munich, pp. 107–115.

Bear, J., 1972. Dynamics of Fluids in Porous Media. Dover.

Bishop, A.W., Alpan, I., Blight, G., Donald, I., 1960. Factors controlling the strength of partly saturated cohesive soils. In: Regional Conference on Shear Strength of Cohesive Soils. Boulder, pp. 503–532.

Bishop, A.W., Blight, G., 1963. Some aspects of effective stress in saturated and partly saturated soils. Geotechnique 13 (3), 177–197. http://dx.doi.org/10.1680/geot.1963.13.3.177.

Bojchevski, A., Matkovic, Y., Günnemann, S., 2017. Robust spectral clustering for noisy data: Modeling sparse corruptions improves latent embeddings. In: Proceedings of the 23rd ACM SIGKDD International Conference on Knowledge Discovery and Data Mining. pp. 737–746. http://dx.doi.org/10.1145/3097983.3098156.

Cai, F., Ugai, K., 2004. Numerical analysis of rainfall effects on slope stability. Int. J. Geomech. 4 (2), 69–78. http://dx.doi.org/10.1061/(ASCE)1532-3641(2004)4:2(69).

Chansorn, R., Chotpantarat, S., Klongvessa, P., 2023. Hydrological model of landslide risk in Huai Nam Phung subbasin, Thailand. Bull. Eng. Geol. Environ. 82 (4), 140. http://dx.doi.org/10.1007/s10064-023-03146-y.

Cho, S.E., 2009. Probabilistic stability analyses of slopes using the ANN-based response surface. Comput. Geotech. 36 (5), 787–797. http://dx.doi.org/10.1016/j.compgeo.2009.01.003.

Chowdhury, R., Xu, D., 1995. Geotechnical system reliability of slopes. Reliab. Eng. Syst. Saf. 47 (3), 141–151. http://dx.doi.org/10.1016/0951-8320(94)00063-T.

Cui, Q., Zhang, L., Chen, X., Cao, Z., Wei, X., Zhang, J., Xu, J., Liu, D., Du, C., 2022. Quantitative risk assessment of landslides with direct simulation of pre-failure to post-failure behaviors. Acta Geotech. 17 (10), 4497–4514. http://dx.doi.org/10.1007/s11440-022-01485-w.

Elia, G., Cotecchia, F., Pedone, G., Vaunat, J., Vardon, P.J., Pereira, C., Springman, S.M., Rouainia, M., Van Esch, J., Koda, E., et al., 2017. Numerical modelling of slope-vegetation-atmosphere interaction: an overview. Q. J. Eng. Geol. Hydrogeol. 50 (3), 249–270. http://dx.doi.org/10.1144/qjegh2016-079.

Ering, P., Kulkarni, R., Kolekar, Y., Dasaka, S.M., Babu, G.S., 2015. Forensic analysis of malin landslide in India. In: IOP Conference Series: Earth and Environmental Science, vol. 26, (1), IOP Publishing, 012040.

Fenton, G.A., Vanmarcke, E.H., 1990. Simulation of random fields via local average subdivision. J. Eng. Mech. 116 (8), 1733–1749. http://dx.doi.org/10.1061/(ASCE)0733-9399(1990)116:8(1733).

Griffiths, D., Fenton, G.A., 2004. Probabilistic slope stability analysis by finite elements. J. Geotech. Geoenviron. Eng. 130 (5), 507–518. http://dx.doi.org/10.1061/(ASCE)1090-0241(2004)130:5(507).

Griffiths, D., Lu, N., 2005. Unsaturated slope stability analysis with steady infiltration or evaporation using elasto-plastic finite elements. Int. J. Numer. Anal. Methods Geomech. 29 (3), 249–267. http://dx.doi.org/10.1002/nag.413.

Gu, X., Wang, L., Ou, Q., Zhang, W., Sun, G.H., 2023. Reliability assessment of rainfall-induced slope stability using Chebyshev-Galerkin-KL expansion and Bayesian approach. Can. Geotech. J. 60 (12), 1909–1922. http://dx.doi.org/10.1139/cgj-2022-0671.

Hicks, M.A., Nuttall, J.D., Chen, J., 2014. Influence of heterogeneity on 3D slope reliability and failure consequence. Comput. Geotech. 61, 198–208. http://dx.doi.org/10.1016/j.compgeo.2014.05.004.

Hicks, M.A., Onisiphorou, C., 2005. Stochastic evaluation of static liquefaction in a predominantly dilative sand fill. Geotechnique 55 (2), 123–133. http://dx.doi.org/10.1680/geot.2005.55.2.123.

Hicks, M.A., Samy, K., 2004. Stochastic evaluation of heterogeneous slope stability. Ital. Geotech. J. 38 (2), 54–66.

Hicks, M.A., Spencer, W.A., 2010. Influence of heterogeneity on the reliability and failure of a long 3D slope. Comput. Geotech. 37 (7–8), 948–955. http://dx.doi.org/10.1016/j.compgeo.2010.08.001.

Hou, R., Chen, N., Hu, G., Han, Z., Liu, E., 2022. Characteristics, mechanisms, and post-disaster lessons of the delayed semi-diagenetic landslide in Hanyuan, Sichuan, China. Landslides 19 (2), 437–449. http://dx.doi.org/10.1007/s10346-021-01751-0.

Huang, J., Griffiths, D., Fenton, G.A., 2010. System reliability of slopes by RFEM. Soils Found. 50 (3), 343–353. http://dx.doi.org/10.3208/sandf.50.343.

Huang, J., Lyamin, A., Griffiths, D., Krabbenhoft, K., Sloan, S., 2013. Quantitative risk assessment of landslide by limit analysis and random fields. Comput. Geotech. 53, 60–67. http://dx.doi.org/10.1016/j.compgeo.2013.04.009.

Hungr, O., Leroueil, S., Picarelli, L., 2014. The varnes classification of landslide types, an update. Landslides 11, 167–194. http://dx.doi.org/10.1007/s10346-013-0436-y.

Jiang, S.H., Huang, J., Griffiths, D., Deng, Z.P., 2022. Advances in reliability and risk analyses of slopes in spatially variable soils: A state-of-the-art review. Comput. Geotech. 141, 104498. http://dx.doi.org/10.1016/j.compgeo.2021.104498.

Jiang, S.-H., Liu, X., Ma, G., Rezania, M., 2023. Stability analysis of heterogeneous infinite slopes under rainfall-infiltration by means of an improved green-ampt model. Can. Geotech. J. (ja), http://dx.doi.org/10.1139/cgj-2023-0203.

Ju, N., Huang, J., He, C., Van Asch, T., Huang, R., Fan, X., Xu, Q., Xiao, Y., Wang, J., 2020. Landslide early warning, case studies from southwest China. Eng. Geol. 279 (20), 105917. http://dx.doi.org/10.1016/j.enggeo.2020.105917.

Le, T.M.H., Gallipoli, D., Sanchez, M., Wheeler, S., 2013. Rainfall-induced differential settlements of foundations on heterogeneous unsaturated soils. Géotechnique 63 (15), 1346–1355. http://dx.doi.org/10.1680/geot.12.P.181.

Le, T.M.H., Gallipoli, D., Sánchez, M., Wheeler, S., 2015. Stability and failure mass of unsaturated heterogeneous slopes. Can. Geotech. J. 52 (11), 1747–1761. http://dx.doi.org/10.1139/cgj-2014-0190.

Le, T.M.H., Sanchez, M., Gallipoli, D., Wheeler, S., 2019. Probabilistic study of rainfall-triggered instabilities in randomly heterogeneous unsaturated finite slopes. Transp. Porous Media 126, 199–222. http://dx.doi.org/10.1007/s11242-018-1140-0.

Li, Y., Hicks, M., Nuttall, J., 2015. Comparative analyses of slope reliability in 3D. Eng. Geol. 196, 12–23. http://dx.doi.org/10.1016/j.enggeo.2015.06.012.

Li, Y., Hicks, M., Vardon, P., 2016. Uncertainty reduction and sampling efficiency in slope designs using 3D conditional random fields. Comput. Geotech. 79, 159–172. http://dx.doi.org/10.1016/j.compgeo.2016.05.027.

Liu, X., Li, D.-Q., Cao, Z.-J., Wang, Y., 2020. Adaptive Monte Carlo simulation method for system reliability analysis of slope stability based on limit equilibrium methods. Eng. Geol. 264, 105384. http://dx.doi.org/10.1016/j.enggeo.2019.105384.

Liu, K., Vardon, P., Hicks, M., 2018. Sequential reduction of slope stability uncertainty based on temporal hydraulic measurements via the ensemble Kalman filter. Comput. Geotech. 95, 147–161. http://dx.doi.org/10.1016/j.compgeo.2017.09.019.

Liu, K., Vardon, P., Hicks, M., Arnold, P., 2017. Combined effect of hysteresis and heterogeneity on the stability of an embankment under transient seepage. Eng. Geol. 219, 140–150. http://dx.doi.org/10.1016/j.enggeo.2016.11.011.

Liu, X., Wang, Y., 2024. Quantifying impacts of precipitation scenarios projected under climate change on annual probability of rainfall-induced landslides at a specific slope. Comput. Geotech. 167, 106063. http://dx.doi.org/10.1016/j.compgeo.2023.106063.

Liu, X., Wang, Y., Leung, A.K., 2023. Numerical investigation of rainfall intensity and duration control of rainfall-induced landslide at a specific slope using slope case histories and actual rainfall records. Bull. Eng. Geol. Environ. 82 (8), 333. http://dx.doi.org/10.1007/s10064-023-03359-1.

Masoudian, M.S., Afrapoli, M.A.H., Tasalloti, A., Marshall, A.M., 2019. A general framework for coupled hydro-mechanical modelling of rainfall-induced instability in unsaturated slopes with multivariate random fields. Comput. Geotech. 115, 103162. http://dx.doi.org/10.1016/j.compgeo.2019.103162.

Mohsan, M., Vardon, P.J., Vossepoel, F.C., 2021. On the use of different constitutive models in data assimilation for slope stability. Comput. Geotech. 138, 104332. http://dx.doi.org/10.1016/j.compgeo.2021.104332.

Mouyeaux, A., Carvajal, C., Bressolette, P., Peyras, L., Breul, P., Bacconnet, C., 2018. Probabilistic stability analysis of an earth dam by stochastic finite element method based on field data. Comput. Geotech. 101, 34–47. http://dx.doi.org/10.1016/j.compgeo.2018.04.017.

Ng, C.W., Qu, C., Ni, J., Guo, H., 2022. Three-dimensional reliability analysis of unsaturated soil slope considering permeability rotated anisotropy random fields. Comput. Geotech. 151, 104944. http://dx.doi.org/10.1016/j.compgeo.2022.104944.

Pan, M., Jiang, S.-H., Liu, X., Song, G.-Q., Huang, J., 2024. Sequential probabilistic back analyses of spatially varying soil parameters and slope reliability prediction under rainfall. Eng. Geol. 328, 107372. http://dx.doi.org/10.1016/j.enggeo.2023.107372.

Phoon, K.-K., Kulhawy, F.H., 1999. Characterization of geotechnical variability. Can. Geotech. J. 36 (4), 612–624. http://dx.doi.org/10.1139/t99-038.

Rodríguez, R., Sánchez, M., Lloret, A., Ledesma, A., 2007. Experimental and numerical analysis of desiccation of a mining waste. Can. Geotech. J. 44 (6), 644–658. http://dx.doi.org/10.1139/T07-016.

Singh, T., Singh, R., Singh, B., Sharma, L., Singh, R., Ansari, M., 2016. Investigations and stability analyses of Malin village landslide of Pune district, Maharashtra, India. Nat. Hazards 81, 2019–2030.

Van Genuchten, M.T., 1980. A closed-form equation for predicting the hydraulic conductivity of unsaturated soils. Soil Sci. Soc. Am. J. 44 (5), 892–898. http://dx.doi.org/10.2136/sssaj1980.03615995004400050002x.

Vardon, P., Liu, K., Hicks, M., 2016. Reduction of slope stability uncertainty based on hydraulic measurement via inverse analysis. Georisk 10 (3), 223–240. http://dx.doi.org/10.1080/17499518.2016.1180400.

Wang, B., Vardon, P., Hicks, M., 2018. Rainfall-induced slope collapse with coupled material point method. Eng. Geol. 239, 1–12. http://dx.doi.org/10.1016/j.enggeo.2018.02.007.

Wang, H., Zou, J., Wu, W., Ni, W., 2023. Assessing unsaturated permeability of loess under multiple rainfalls. Eng. Geol. 324, 107280. http://dx.doi.org/10.1016/j.enggeo.2023.107280.

Yang, Y., Chen, G., Meng, X., Bian, S., Chong, Y., Shi, W., Jiang, W., Jin, J., Li, C., Mu, X., et al., 2022. Analysis of the microseismicity characteristics in landslide dam failure flume tests: implications for early warning and dynamics inversion. Landslides 19 (4), 789–808. http://dx.doi.org/10.1007/s10346-021-01783-6.

Zandarín, M.T., Oldecop, L.A., Rodríguez, R., Zabala, F., 2009. The role of capillary water in the stability of tailing dams. Eng. Geol. 105 (1–2), 108–118. http://dx.doi.org/10.1016/j.enggeo.2008.12.003.

Zhang, J., Huang, H., 2016. Risk assessment of slope failure considering multiple slip surfaces. Comput. Geotech. 74, 188–195. http://dx.doi.org/10.1016/j.compgeo.2016.01.011.

Zhang, J., Huang, H.W., Zhang, L.M., Zhu, H.H., Shi, B., 2014. Probabilistic prediction of rainfall-induced slope failure using a mechanics-based model. Eng. Geol. 168, 129–140. http://dx.doi.org/10.1016/j.enggeo.2013.11.005.

Zhu, T., 2014. Some useful numbers on the engineering properties of materials-GEOL 615. https://cpb-us-e1.wpmucdn.com/sites.psu.edu/dist/1/57960/files/2016/10/some-useful-numbers-1g1rkuu.pdf. (Accessed 1 March 2024).